Observation of edge and bulk states in a three-site Kitaev chain

ten Haaf, Sebastiaan L.D.; Zhang, Yining; Wang, Qingzhen; Bordin, Alberto; Liu, Chun Xiao; Kulesh, Ivan; Sietses, Vincent P.M.; Prosko, Christian G.; Wimmer, Michael; Goswami, Srijit

DOI
10.1038/s41586-025-08892-5

Publication date
2025

Document Version
Final published version

Published in
Nature

Observation of edge and bulk states in a three-site Kitaev chain

https://doi.org/10.1038/s41586-025-08892-5

Received: 23 October 2024

Accepted: 12 March 2025

Published online: 30 April 2025

Check for updates

Sebastiaan L. D. ten Haaf[1], Yining Zhang[1], Qingzhen Wang[1], Alberto Bordin[1], Chun-Xiao Liu[1], Ivan Kulesh[1], Vincent P. M. Sietses[1], Christian G. Prosko[1], Di Xiao[2], Candice Thomas[2], Michael J. Manfra[2,3,4], Michael Wimmer[1] & Srijit Goswami[1]✉

A chain of quantum dots (QDs) in semiconductor–superconductor hybrid systems can form an artificial Kitaev chain hosting Majorana bound states (MBSs)[1–3]. These zero-energy states are expected to be localized on the edges of the chain[4], at the outermost QDs. The remaining QDs, comprising the bulk, are predicted to host an excitation gap that protects the MBSs at the edges from local on-site perturbations. Here we demonstrate this connection between the bulk and edges in a minimal system, by engineering a three-site Kitaev chain in a two-dimensional electron gas. Through direct tunnelling spectroscopy on each site, we show that the appearance of stable zero-bias conductance peaks at the outer QDs is correlated with the presence of an excitation gap in the middle QD. Furthermore, we show that this gap can be controlled by applying a superconducting phase difference between the two hybrid segments and that the MBSs are robust only when the excitation gap is present. We find a close agreement between experiments and the original Kitaev model, thus confirming key predictions for MBSs in a three-site chain.

The study of topology in condensed matter has generated interest in engineering quantum phases hosting modes that are robust to external perturbations[5–8]. In particular, realizations of one-dimensional topological superconductors[9,10] are expected to host robust edge modes known as Majorana bound states (MBSs), first predicted by the Kitaev chain model[4]. These states are separated by a bulk region with an excitation gap that prevents local perturbations from affecting the zero-energy modes at the edges, resulting from the so-called bulk-edge correspondence[11,12]. Experimentally, much effort has gone towards top-down approaches to engineer these systems by coupling semiconductors with superconductors[13]. However, microscopic disorder in these systems complicates the study of MBSs[14–19]. Alternatively, bottom-up approaches aim to mitigate this, for example, by constructing a Kitaev chain atom-by-atom[20,21] or by engineering arrays of quantum dots (QDs) in semiconductor–superconductor hybrids[1,3]. An implementation of the latter approach with two QDs[2] was recently demonstrated in nanowires[22] and two-dimensional electron gases (2DEGs)[23]. However, in a two-site chain, neither QD site can be associated with a bulk. By contrast, a chain with three QDs constitutes a minimal system in which we can distinguish distinct edges (the outer QDs) hosting MBSs and a bulk (the middle QD). Recent work demonstrated stable zero-energy modes in such a system[24], but was unable to investigate the density of states of the middle QD.

In this work, we realize a three-site Kitaev chain in an InSbAs 2DEG and perform a detailed study of the bulk and edge states in the system. Crucially, ohmic contacts attached to each QD allow us to directly probe the density of states at all three sites. By controlling the interdot couplings and the superconducting phase difference, we can tune the system such that robust zero-bias conductance peaks (ZBPs) arise on the outer QDs. We demonstrate that these correlated ZBPs at the edges are accompanied by an excitation gap in the middle QD. This gap can be controlled by tuning the phase difference between the superconductors, allowing us to establish a clear correlation between the presence of isolated zero-energy edge modes and their robustness against on-site perturbations. In particular, access to every QD allows us to track how the weight of the Majorana wavefunction evolves across each site as the device parameters are varied. Finally, we construct a phase diagram of a finite Kitaev chain by identifying regions in parameter space in which ZBPs are observed. Through continuous control over the interdot couplings and the QD electrochemical potential energies, we show that this region grows when extending from a two-site chain to a three-site chain. These findings are in close agreement with the original Kitaev model and provide important insights for more advanced experiments with MBSs.

The Kitaev model for a three-site QD chain

Implementing a Kitaev chain on a QD array requires control over the electrochemical potential energy of each site and the amplitudes of couplings between neighbouring sites. This can be engineered by coupling spin-polarized QDs with Andreev bound states in semiconductor–superconductor hybrids[22]. Here a hopping interaction (t) occurs through elastic co-tunnelling (ECT). Crossed Andreev reflection (CAR) provides a pairing interaction (Δ) by the creation or breaking of Cooper pairs in the superconductor[25–28]. Intrinsic spin–orbit coupling allows for CAR between neighbouring sites with the same spin, or ECT between

[1]QuTech and Kavli Institute of NanoScience, Delft University of Technology, Delft, The Netherlands. [2]Department of Physics and Astronomy, Purdue University, West Lafayette, IN, USA. [3]Elmore School of Electrical and Computer Engineering, Purdue University, West Lafayette, IN, USA. [4]School of Materials Engineering, Purdue University, West Lafayette, IN, USA. ✉e-mail: s.goswami@tudelft.nl

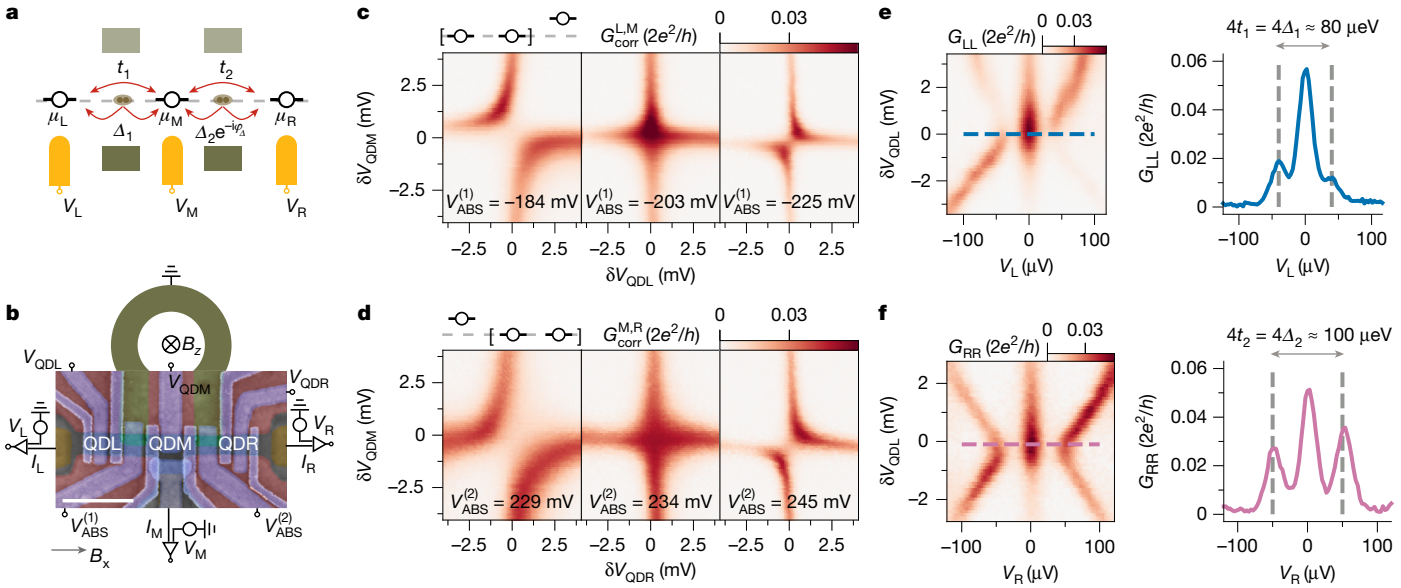

Fig. 1 | Device, model and characterization of two-site pairs. a, Energy-level diagram of the three-site Kitaev chain model, indicating the different interdot couplings in the system. **b**, Scanning electron micrograph of a copy of the device. Scale bar, 500 nm. Positions of gate-defined QDs are indicated. Two superconducting strips are connected in a loop with a diameter of 10 μm and kept grounded (not drawn to scale). The d.c. circuit diagram shows a four-terminal measurement set-up (a full circuit diagram, including resonators for reflectometry measurements, is shown in Extended Data Fig. 1). **c**, Measured correlated conductance $G^{L,M}_{corr} = \sqrt{G_{LL} \cdot G_{MM}}$ as a function of V_{QDL} and V_{QDM}, on varying $V^{(1)}_{ABS}$. The notation δV_{QDi} refers to the voltage set with respect to the nearest charge degeneracy point. **d**, Measured correlated conductance $G^{M,R}_{corr} = \sqrt{G_{MM} \cdot G_{RR}}$ as a function of V_{QDR} and V_{QDM}, on varying $V^{(2)}_{ABS}$. The disappearance of the avoided crossing in **c** (middle) and **d** (middle) signifies satisfying the two-site sweet spot conditions. **e**, Finite bias spectroscopy measurement of G_{LL} at the left QD pair sweet spot, while varying V_{QDL}. **f**, Finite bias spectroscopy of G_{RR} at the right QD pair sweet spot, while varying V_{QDR}. Line traces taken at the minima of the higher-energy excitations allow for estimating the experimental coupling amplitudes at the sweet spots (**e**,**f** (right)). Results presented use the ↓↑↑ spin configuration. Further characterization of the two-site pairs is presented in Extended Data Fig. 4.

neighbours with opposite spin, otherwise forbidden because of spin conservation[29]. When the Zeeman energy in each QD is large ($E_z \gg t, \Delta$), a single spin species dominates transport at charge degeneracy points, thus emulating the Kitaev model[30,31]. To distinguish different charge configurations for the three QDs, the spin configuration is used as a label. The energy-level diagram for a chain with three QDs is shown in Fig. 1a. Electrochemical potential energies are denoted as μ_i, where $i \in \{L, M, R\}$ refers to the left, middle or right QD, respectively. The effective couplings between the left and middle QD, t_1 and Δ_1, and between the middle and right QD, t_2 and Δ_2, are indicated. Uncoupled MBSs arise on the outer QDs at a so-called sweet spot in parameter space, when all three QDs are aligned with the Fermi level of the superconductor ($\mu_i = 0$) and the interdot couplings are equal in amplitude pairwise ($|t_1| = |\Delta_1|$, $|t_2| = |\Delta_2|$). Notably, the coupling amplitudes are not necessarily purely real in a system with more than two QDs[3,24,32]. A gauge degree of freedom allows us to take t_1, t_2 and Δ_1 to be real and assign a complex phase only to Δ_2, denoted as ϕ_Δ. We compare our experimental results to this three-site Kitaev model. Numerical simulations of the conductance are performed using a scattering matrix approach with experimentally extracted parameters. A more detailed description is included in the Methods.

Device and measurement set-up

A scanning electron micrograph of a copy of the measured device is shown in Fig. 1b. Large gates (red) define a quasi-one-dimensional channel across two thin aluminium strips that are connected by a continuous loop. An external magnetic field B_z applied perpendicular to the loop controls the superconducting phase difference ϕ_{SC} between the two strips, with a flux period of 28 μT (Extended Data Fig. 1). The energy of the ABSs in the left and right hybrid regions can be tuned by voltages $V^{(1)}_{ABS}$ and $V^{(2)}_{ABS}$, respectively. Narrow gates define three QDs in the channel. Their electrochemical potentials are controlled by voltages V_{QDL}, V_{QDM} and V_{QDR}, respectively. Voltages applied to a left, middle and right lead (V_L, V_M and V_R) can be varied, and the currents in each lead (I_L, I_M and I_R) can be measured independently. Lock-in amplifiers allow for direct measurements of the local conductance at each probe ($G_{ii} = \frac{dI_i}{dV_i}$, $i \in \{L, M, R\}$). To capture features appearing simultaneously on multiple sites, the correlated conductance $G^{i,j}_{corr} = \sqrt{G_{ii} \cdot G_{jj}}$ is extracted when relevant. Results in the main text are obtained using a single orbital in each QD, characterized in Extended Data Figs. 2 and 3. All measurements are performed at $B_x = 200$ mT, applied perpendicular to the spin–orbit field in these systems[33].

Tuning the two-site pairs

Tuning a three-site Kitaev chain amounts to pairwise tuning of the two-site sweet spots ($t_i = \Delta_i$) (ref. 1). These conditions can be inferred from zero-bias charge stability diagrams (CSDs) for the two pairs of QD resonances[2], using the methods used for two-site Kitaev chains[22,23,34]. First, we obtain CSDs for the left and middle QDs, while keeping the right QD in Coulomb blockade (Fig. 1c). The measurement is repeated as $V^{(1)}_{ABS}$ is varied, to locate when the avoided crossing in the CSD changes direction. A diagonal avoided crossing indicates $\Delta_1 > t_1$ (Fig. 1c (left)), whereas an antidiagonal avoided crossing results from $t_1 > \Delta_1$ (Fig. 1c (right)). At an intermediate value of $V^{(1)}_{ABS}$, the desired $t_1 = \Delta_1$ condition is satisfied, in which the avoided crossing disappears (Fig. 1c (middle)). This procedure is repeated for the middle and right QDs, now varying $V^{(2)}_{ABS}$. This is seen in Fig. 1d, in which $t_2 = \Delta_2$ is satisfied in Fig. 1d (middle).

It has been shown that robust, correlated ZBPs arise at these two-site sweet spots[22,23,34]. These are manifestations of localized MBSs, in the two-site case referred to as 'poor man's Majoranas' as their stability is limited to single QD perturbations[2]. We demonstrate this stability of the ZBPs for each pair of QDs. In Fig. 1e, we measure G_{LL} as QDL is detuned,

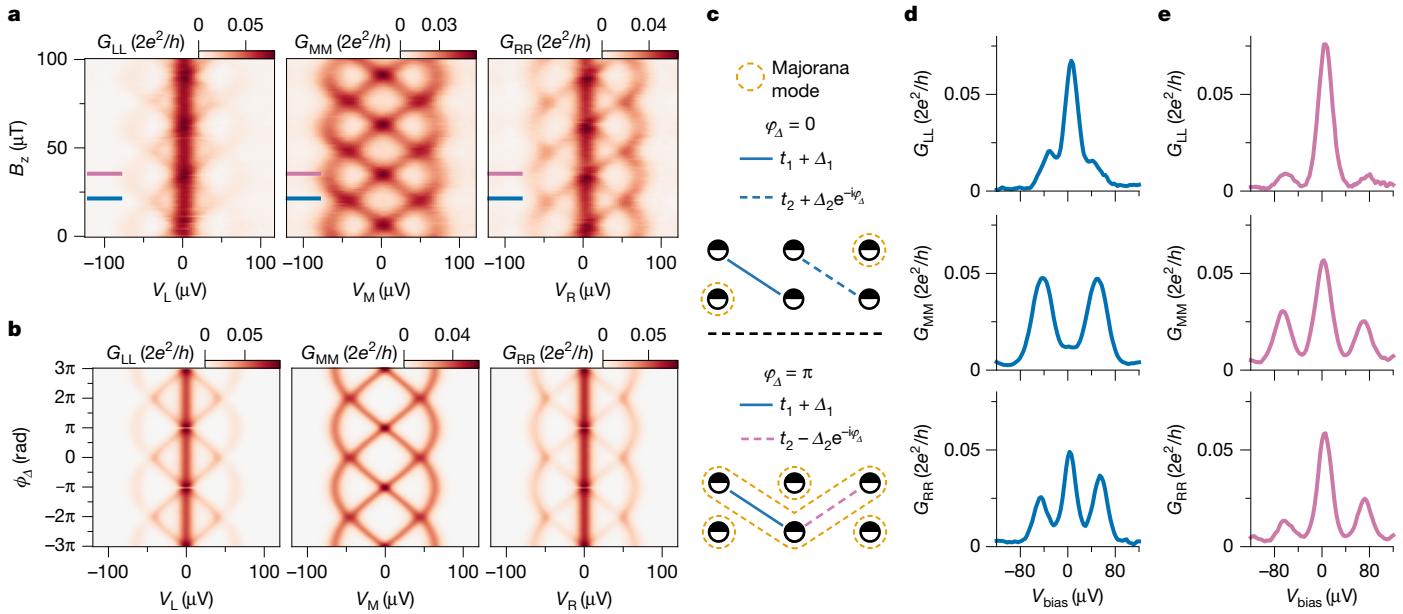

Fig. 2 | Phase control at the three-site sweet spot. a, Measured conductances G_{LL}, G_{MM} and G_{RR} at the sweet spot configuration obtained in Fig. 1, as a function of magnetic field B_z applied perpendicular to the superconducting loop. When either of the outer QDs is set off-resonance, B_z no longer affects the conductance spectra (Extended Data Fig. 4), indicating the observed behaviour here is an effect on the full three-site chain. **b**, Evolution of numerically calculated conductances in a three-site Kitaev chain on varying ϕ_Δ. Numerical parameters used are $\mu_L = \mu_M = \mu_R = 0$, $t_1 = \Delta_1 = 20$ μeV and $t_2 = \Delta_2 = 25$ μeV (matching estimations in Fig. 1e,f). **c**, Visual representation of the three-site Kitaev chain Hamiltonian at $\phi_\Delta = 0$ and $\phi_\Delta = \pi$, in the Majorana basis. Connecting lines indicate non-zero coupling terms between Majoranas for each case. Dashed circles highlight the distribution of uncoupled Majorana modes (further detailed in the Methods). **d**, Line traces taken from **a** at $B_z = 21.4$ μT, corresponding to $\phi_\Delta = 0$. The finite conductance at zero bias in **d** (middle) can be largely attributed to thermal broadening, shown in Extended Data Fig. 5. **e**, Line traces taken at $B_z = 35.4$ μT, corresponding to $\phi_\Delta = \pi$.

for the configuration in Fig. 1c (middle). Similarly, G_{RR} is measured for the configuration in Fig. 1d (middle) on varying V_{QDR} (Fig. 1f). In both cases, we find robust zero energy states. At the charge degeneracy point, the higher-energy excitations provide an estimate[2] for $t_1 = \Delta_1 \approx 20$ μeV (Fig. 1e (right)) and $t_2 = \Delta_2 \approx 25$ μeV (Fig. 1f (right)). These measurements are in good agreement with the theoretical spectrum for well-polarized QDs[30,35,36], signifying that the ingredients for a full three-site Kitaev chain are present.

Phase control and the bulk excitation gap

With t and Δ balanced for each QD pair, the full three-site chain can be investigated. Now the phase difference between the superconductors becomes a relevant parameter as it can affect the relative phase between the interdot couplings[1,3,24]. To investigate this, we set $V_{ABS}^{(1)}$ and $V_{ABS}^{(2)}$ to the sweet spot values obtained in Fig. 1 and set the QDs to their charge degeneracy points. The conductance spectrum of each QD is then measured as a function of B_z (Fig. 2a). ZBPs are continuously observed on the outer QDs (G_{LL} and G_{RR}), whereas the middle QD (G_{MM}) hosts higher-energy excitations that move down to zero energy periodically. This period in B_z is equal to the period of ϕ_{SC} (28 μT) measured for the bare superconducting junction. We compare this behaviour to numerically calculated conductance spectra (Fig. 2b) of the three-site Kitaev chain as a function of ϕ_Δ, using the experimental coupling amplitudes estimated in Fig. 1. A clear correspondence to the experimental result is obtained. When the phase is 0 (modulo 2π), ZBPs are present in G_{LL} and G_{RR}, whereas an excitation gap is present in G_{MM}. As the phase is tuned towards π, finite-energy excitations lower in energy until the excitation gap is closed.

The observed behaviour can be understood when considering the Kitaev chain model in the Majorana basis (Methods), shown in Fig. 2c. Each QD site can be represented by two Majoranas. For $\phi_\Delta = 0$, an uncoupled Majorana arises only on the left and right sites, while the middle site is gapped. Experimental line traces (Fig. 2d) at the corresponding magnetic field value are in agreement with this interpretation. A ZBP is present in G_{LL} and G_{RR} (Fig. 2d, top and middle), whereas G_{MM} only shows excitations at higher bias (Fig. 2d, middle). This is a direct indication of the localization of the MBS wavefunctions on the outer QDs. In stark contrast, at a magnetic field that corresponds to $\phi_\Delta = \pi$, ZBPs are found on all three sites (Fig. 2e). Here, the coupling between neighbouring Majoranas is rearranged (Fig. 2c), resulting in four uncoupled Majorana modes: one localized on each site, and an additional delocalized mode extending across all three sites. Consequently, every site has a finite density of states at zero bias, leading to the observed conductances.

Shifting the Majorana wavefunctions

The presence or absence of the excitation gap in the middle QD has direct consequences for the robustness of the ZBPs on the outer QDs. In an ideal system, the energy of each isolated MBS cannot be lifted because of particle–hole symmetry. Only an overlap between the two MBSs can achieve this, which is prevented by an excitation gap. As shown above, the excitation gap is affected by ϕ_Δ. The robustness of the ZBPs is, therefore, also expected to be phase-dependent. We compare the conductance spectra obtained at B_z values corresponding to $\phi_\Delta = 0$ and $\phi_\Delta = \pi$, in which the excitation gap is either present or closed.

We first consider the spectra at $\phi_\Delta = 0$, on detuning QDL (Fig. 3a). The ZBP in G_{LL} remains at zero bias, whereas a ZBP gradually appears in G_{MM}. The conductances at zero bias are expected to be proportional to the density of the Majorana wavefunction at each site (Extended Data Fig. 8). Figure 3b shows extracted line traces at zero bias. As QDL is detuned, G_{LL} gradually reduces, whereas G_{MM} simultaneously increases. This happens because the weight of the Majorana wavefunction shifts from the left to the middle QD[37] (Fig. 3c). Finally, we see that the spectrum at QDR is hardly affected, a consequence of the isolation of the MBS on this site.

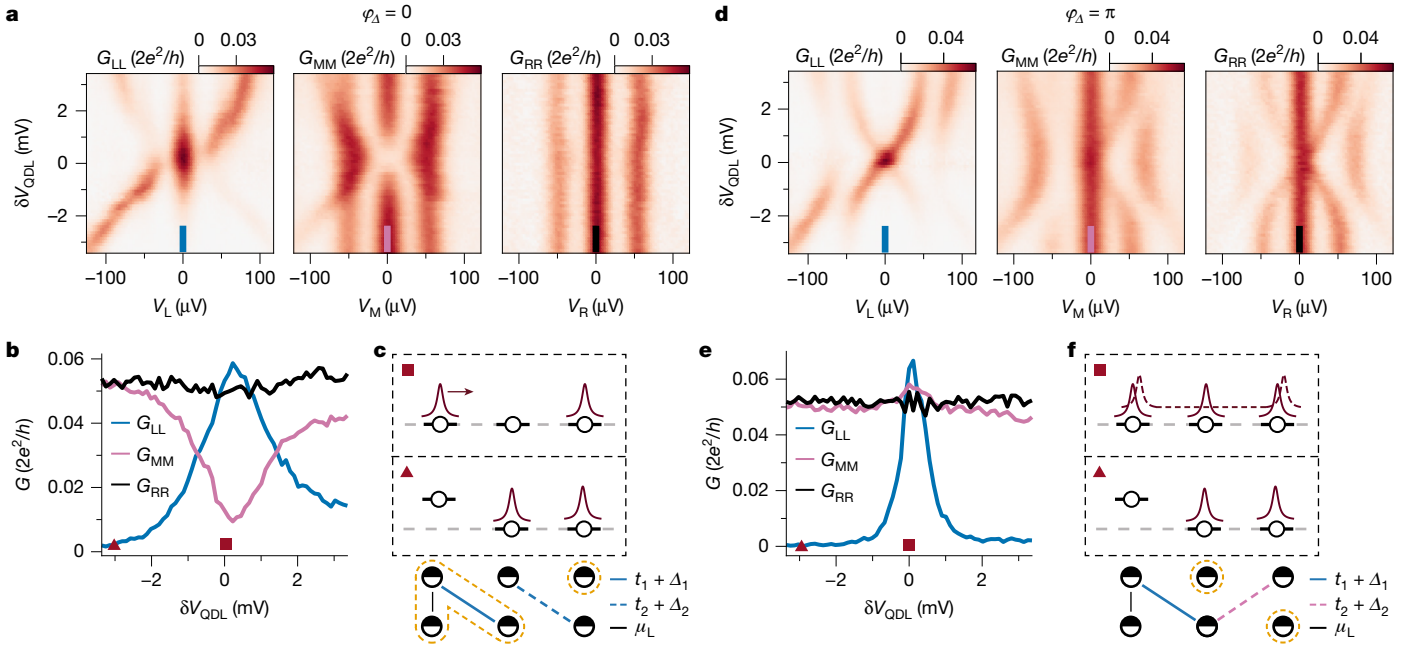

Fig. 3 | Bulk protection of the MBS wavefunctions. a, Measured conductances with $B_z = 21.4$ μT (corresponding to $\phi_\Delta = 0$ in Fig. 2) when sweeping V_{QDL} around the charge degeneracy point. Measurements are performed with the same gate configuration as in Fig. 2. The ZBP in G_{LL} gradually decreases in height, whereas a ZBP in G_{MM} gradually appears. **b**, Zero-bias line traces of conductance along indicated paths in **a**. **c**, Visual representation of the measurements in **b**, showing the MBS wavefunctions when V_{QDL} is on resonance (square) or off-resonance (triangle). The bottom schematic shows the effect of introducing the coupling term μ_L, in the picture introduced in Fig. 2. **d**, Repetition of the measurement in **a** with $B_z = 35.4$ μT (corresponding to $\phi_\Delta = \pi$). The ZBP in G_{LL} now splits from zero energy as V_{QDL} is detuned. The ZBPs in G_{MM} and G_{RR} remain, as the system effectively becomes a two-site chain as V_{QDL} is detuned. **e**, Zero-bias line traces of conductance along indicated paths in **d**. **f**, Visual representation of the measurements in **e**, detailed in text. The smooth control over ϕ_Δ through B_z allows for comparing these conductance spectra at any intermediate phase, shown in Extended Data Fig. 6.

The spectra at $\phi_\Delta = \pi$, in which the gap in QDM is closed, have a markedly different behaviour (Fig. 3d). The ZBP in G_{LL} now splits immediately in energy as QDL is detuned. This is expected because MBSs in the system now directly overlap and are thus no longer robust to detuning. Line traces at zero bias (Fig. 3e) show two important features. First, G_{LL} now drops faster compared with those in Fig. 3b, because of the lack of protection. Second, the ZBPs in both G_{MM} and G_{RR} are now unaffected by the detuning of the left QD. This can again be understood in terms of the MBS wavefunctions (Fig. 3f), in which detuning the left QD now fuses the localized MBS on QDL with the delocalized MBS extending across the chain[32,38,39]. These observations, and conductance spectra obtained for additional combinations of QD detunings, again show a striking agreement with numerical simulations (Extended Data Figs. 7 and 9).

ZBPs outside the sweet spot

In the previous sections, the system was characterized at fine-tuned sweet spots at which ZBPs appear on the outer QDs. It is expected that ZBPs should also be present away from these sweet spots. This follows from a key property of the Kitaev model, in which the region in parameter space that hosts MBSs grows as the number of sites N is increased. For finite chains, MBSs are fully localized at the edges only at the $t_i = \Delta_i$ sweet spot[40]. However, ZBPs arising from delocalized MBSs are expected away from this point. To study this, it is instructive to extract zero-energy solutions of the Kitaev chain as a function of μ and t, for fixed Δ. An exact analytical expression for the zero-energy solutions exists for any N (ref. 40), shown in Fig. 4a. For $N = 2$, the solutions lie on a single hyperbola, with a vertex at $t = \Delta$, $\mu = 0$ (that is, the two-site sweet spot). For each odd N, $\mu = 0$ is always a solution[41] (see $N = 3$). As N increases, the number of solutions increases and gradually fills the region in which $|\mu| < 2t$. As $N \to \infty$, this region is filled with states exponentially close to zero energy, ultimately creating a topological phase within which the MBSs are always localized at the edges. The zero-energy solutions can be studied by measuring zero-bias conductances on each QD while varying both interdot couplings and the QD electrochemical potential energies. Figure 4b,c shows numerical simulations for $N = 2$ and $N = 3$, respectively.

Experimentally, this parameter space is only indirectly accessible, as t_i and Δ_i are not controlled independently. However, starting with the hybrid gates at their sweet spot value (denoted $\delta V_{ABS}^{(i)} = 0$) and sweeping both simultaneously, the system can be smoothly tuned between $t_i < \Delta_i$ and $t_i > \Delta_i$ regimes (full procedure in Extended Data Fig. 10). Figure 4d shows this for the left and middle QD pairs. Here, the conductance features meeting at $\delta V_{ABS}^{(i)} = 0$ agree qualitatively with the behaviour expected from Fig. 4b. Instead of extending linearly as $t_1 > \Delta_1$, the feature saturates in μ_i, because t_1 does not increase independently of Δ_1 in these experiments. The finite conductance 'tail' at $\mu_i = 0$ here is a consequence of both t and Δ decreasing in amplitude (Extended Data Fig. 10), which is not captured by the theory model.

Next, the measurement is performed for the full chain, sweeping simultaneously both hybrid gates against detuning all three QDs (Fig. 4e). The appearance of the additional conductance feature along $\mu_i = 0$ marks the first step of the growth into a topological phase in this discrete system and agrees well with the Kitaev chain model in a large parameter space. Finally, these measurements allow us to qualitatively visualize the increase in stability of the MBSs as the chain is extended[24]. We find that conductance decays more slowly for the three-site chain compared with the two-site chain as one moves away from the sweet spot (marked by white 'x') in any direction.

Conclusions

In summary, we have realized a three-site Kitaev chain by coupling three QDs via two semiconductor–superconductor regions. We find

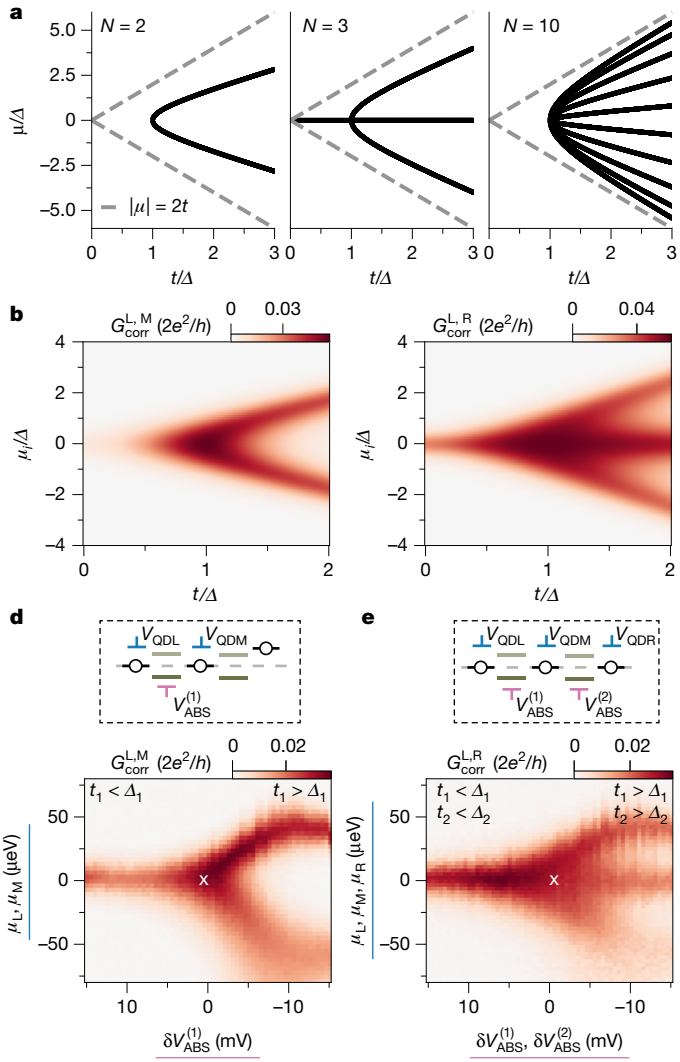

Fig. 4 | The finite Kitaev chain's phase space. a, Analytical zero-energy solutions to the N-site Kitaev chain with fixed Δ, for different N (reproduced from ref. 40). The grey dashed line indicates the boundary of the topological phase formed at $N \to \infty$. **b**,**c**, Numerically calculated conductance is shown for $N = 2$ (**b**) and $N = 3$ (**c**). Here, $\Delta = 20$ μeV. **d**, Measured correlated conductance when sweeping $V^{(1)}_{ABS}$ against V_{QDL} and V_{QDM} (converted to μ_L and μ_M using QD leverarms). **e**, Measured correlated conductance when sweeping both $V^{(1)}_{ABS}$ and $V^{(2)}_{ABS}$ against V_{QDL}, V_{QDM} and V_{QDR}. White 'x' marks the point in parameter space referred to as the sweet spot for the two- and three-site chains. In **d** and **e**, the x-axis is flipped to match numerical simulations. The ↑↑↑ spin configuration is used. Measurements are reproduced in Extended Data Fig. 11.

that the phase difference between the superconductors controls the relative phase between the interdot couplings, and thereby the energy spectrum of the system. This finding is particularly relevant for the study of zero energy modes in longer chains[42,43], where control over these phases becomes crucial[1,32]. By appropriately tuning the phase, we show that the appearance of ZBPs on the outer QDs is accompanied by an excitation gap in the middle QD, evidence of the zero-energy modes being localized at the edges. We further demonstrate that detuning of the QDs in the chain allows one to smoothly transfer the weight of the Majorana wavefunction between different sites. This kind of spatial manipulation of MBSs is a crucial requirement in gate-based braiding proposals for realizing a Majorana qubit[44,45]. Overall, our experiments agree well with the predictions of the Kitaev model in a wide parameter space and are an important step towards studies that require a reliable way to produce robust, localized Majorana bound states[46–48].

Online content

Any methods, additional references, Nature Portfolio reporting summaries, source data, extended data, supplementary information, acknowledgements, peer review information; details of author contributions and competing interests; and statements of data and code availability are available at https://doi.org/10.1038/s41586-025-08892-5.

1. Sau, J. D. & Sarma, S. D. Realizing a robust practical Majorana chain in a quantum-dot-superconductor linear array. *Nat. Commun.* **3**, 964 (2012).
2. Leijnse, M. & Flensberg, K. Parity qubits and poor man's Majorana bound states in double quantum dots. *Phys. Rev. B* **86**, 134528 (2012).
3. Fulga, I. C., Haim, A., Akhmerov, A. R. & Oreg, Y. Adaptive tuning of Majorana fermions in a quantum dot chain. *New J. Phys.* **15**, 045020 (2013).
4. Kitaev, A. Y. Unpaired Majorana fermions in quantum wires. *Phys. Usp.* **44**, 131 (2001).
5. Kane, C. L. & Mele, E. J. Quantum spin Hall effect in graphene. *Phys. Rev. Lett.* **95**, 226801 (2005).
6. Hasan, M. Z. & Kane, C. L. Colloquium: topological insulators. *Rev. Mod. Phys.* **82**, 3045–3067 (2010).
7. Qi, X.-L. & Zhang, S.-C. Topological insulators and superconductors. *Rev. Mod. Phys.* **83**, 1057–1110 (2011).
8. Alicea, J. New directions in the pursuit of Majorana fermions in solid state systems. *Rep. Prog. Phys.* **75**, 076501 (2012).
9. Lutchyn, R. M., Sau, J. D. & Sarma, S. D. Majorana fermions and a topological phase transition in semiconductor-superconductor heterostructures. *Phys. Rev. Lett.* **105**, 077001 (2010).
10. Oreg, Y., Refael, G. & Oppen, F.von Helical liquids and Majorana bound states in quantum wires. *Phys. Rev. Lett.* **105**, 177002 (2010).
11. Halperin, B. I. Quantized Hall conductance, current-carrying edge states, and the existence of extended states in a two-dimensional disordered potential. *Phys. Rev. B* **25**, 2185–2190 (1982).
12. Wen, X.-G. Topological orders and edge excitations in fractional quantum Hall states. *Adv. Phys.* **44**, 405–473 (1995).
13. Prada, E. et al. From Andreev to Majorana bound states in hybrid superconductor–semiconductor nanowires. *Nat. Rev. Phys.* **2**, 575–594 (2020).
14. Liu, C.-X., Sau, J. D., Stanescu, T. D. & Sarma, S. D. Andreev bound states versus Majorana bound states in quantum dot-nanowire-superconductor hybrid structures: Trivial versus topological zero-bias conductance peaks. *Phys. Rev. B* **96**, 075161 (2017).
15. Reeg, C., Dmytruk, O., Chevallier, D., Loss, D. & Klinovaja, J. Zero-energy Andreev bound states from quantum dots in proximitized Rashba nanowires. *Phys. Rev. B* **98**, 245407 (2018).
16. Vuik, A., Nijholt, B., Akhmerov, A. R. & Wimmer, M. Reproducing topological properties with quasi-Majorana states. *SciPost Phys.* **7**, 061 (2019).
17. Pan, H. & Sarma, S. D. Physical mechanisms for zero-bias conductance peaks in Majorana nanowires. *Phys. Rev. Res.* **2**, 013377 (2020).
18. Sarma, S. D. & Pan, H. Disorder-induced zero-bias peaks in Majorana nanowires. *Phys. Rev. B* **103**, 195158 (2021).
19. Kouwenhoven, L. Perspective on Majorana bound-states in hybrid superconductor-semiconductor nanowires. *Mod. Phys. Lett. B* **39**, 2540002 (2025).
20. Li, J. et al. Topological superconductivity induced by ferromagnetic metal chains. *Phys. Rev. B* **90**, 235433 (2014).
21. Nadj-Perge, S. et al. Observation of Majorana fermions in ferromagnetic atomic chains on a superconductor. *Science* **346**, 602–607 (2014).
22. Dvir, T. et al. Realization of a minimal Kitaev chain in coupled quantum dots. *Nature* **614**, 445–450 (2023).
23. Haaf, S. L. D. et al. A two-site Kitaev chain in a two-dimensional electron gas. *Nature* **630**, 329–334 (2024).
24. Bordin, A. et al. Enhanced Majorana stability in a three-site Kitaev chain. *Nat. Nanotechnol.* https://doi.org/10.1038/s41565-025-01894-4 (2025).
25. Liu, C.-X., Wang, G., Dvir, T. & Wimmer, M. Tunable superconducting coupling of quantum dots via Andreev bound states in semiconductor-superconductor nanowires. *Phys. Rev. Lett.* **129**, 267701 (2022).
26. Bordin, A. et al. Tunable crossed Andreev reflection and elastic cotunneling in hybrid nanowires. *Phys. Rev. X* **13**, 031031 (2023).
27. Bordin, A. et al. Crossed andreev reflection and elastic cotunneling in three quantum dots coupled by superconductors. *Phys. Rev. Lett.* **132**, 056602 (2024).
28. Liu, Z.-H., Zeng, C. & Xu, H. Q. Coupling of quantum-dot states via elastic cotunneling and crossed Andreev reflection in a minimal Kitaev chain. *Phys. Rev. B* **110**, 115302 (2024).
29. Wang, G. et al. Singlet and triplet Cooper pair splitting in hybrid superconducting nanowires. *Nature* **612**, 448–453 (2022).
30. Tsintzis, A., Souto, R. S. & Leijnse, M. Creating and detecting poor man's Majorana bound states in interacting quantum dots. *Phys. Rev. B* **106**, L201404 (2022).
31. Luethi, M., Legg, H. F., Loss, D. & Klinovaja, J. From perfect to imperfect poor man's majoranas in minimal kitaev chains. *Phys. Rev. B* **110**, 245412 (2024).
32. Liu, C.-X. et al. Scaling up a sign-ordered Kitaev chain without magnetic flux control. *Phys. Rev. Res.* **7**, L012045 (2025).
33. Wang, Q. et al. Triplet correlations in Cooper pair splitters realized in a two-dimensional electron gas. *Nat. Commun.* **14**, 4876 (2023).
34. Zatelli, F. et al. Robust poor man's Majorana zero modes using Yu-Shiba-Rusinov states. *Nat. Commun.* **15**, 7933 (2024).
35. Bozkurt, A. M. et al. Interaction-induced strong zero modes in short quantum dot chains with time-reversal symmetry. Preprint at arxiv.org/abs/2405.14940 (2024).
36. Liu, C.-X. et al. Enhancing the excitation gap of a quantum-dot-based Kitaev chain. *Commun. Phys.* **7**, 235 (2024).

37. Pandey, B., Gupta, G. K., Alvarez, G., Okamoto, S. & Dagotto, E. Diabatic error and propagation of Majorana zero modes in interacting quantum dots systems. Preprint at arxiv.org/abs/2501.06288 (2025).
38. Pandey, B., Okamoto, S. & Dagotto, E. Nontrivial fusion of Majorana zero modes in interacting quantum-dot arrays. *Phys. Rev. Res.* **6**, 033314 (2024).
39. Pandey, B., Kaushal, N., Alvarez, G. & Dagotto, E. Majorana zero modes in Y-shape interacting Kitaev wires. *NPJ Quantum Mater.* **8**, 51 (2023).
40. Leumer, N., Marganska, M., Muralidharan, B. & Grifoni, M. Exact eigenvectors and eigenvalues of the finite Kitaev chain and its topological properties. *J. Phys. Condens. Matter* **32**, 445502 (2020).
41. Ezawa, M. Even-odd effect on robustness of Majorana edge states in short Kitaev chains. *Phys. Rev. B* **109**, L161404 (2024).
42. Luethi, M., Legg, H. F., Loss, D. & Klinovaja, J. The fate of poor man's Majoranas in the long Kitaev chain limit. Preprint at arxiv.org/abs/2408.10030 (2025).
43. Svensson, V. & Leijnse, M. Quantum dot based Kitaev chains: Majorana quality measures and scaling with increasing chain length. *Phys. Rev. B* **110**, 155436 (2024).
44. Alicea, J., Oreg, Y., Refael, G., Oppen, F. & Fisher, M. P. A. Non-Abelian statistics and topological quantum information processing in 1D wire networks. *Nat. Phys.* **7**, 412–417 (2011).
45. Boross, P. & Pályi, A. Braiding-based quantum control of a Majorana qubit built from quantum dots. *Phys. Rev. B* **109**, 125410 (2024).
46. Tsintzis, A., Souto, R. S., Flensberg, K., Danon, J. & Leijnse, M. Majorana qubits and non-abelian physics in quantum dot–based minimal Kitaev chains. *PRX Quantum* **5**, 010323 (2024).
47. Liu, C.-X., Pan, H., Setiawan, F., Wimmer, M. & Sau, J. D. Fusion protocol for Majorana modes in coupled quantum dots. *Phys. Rev. B* **108**, 085437 (2023).
48. Pan, H., Sarma, S. D. & Liu, C.-X. Rabi and Ramsey oscillations of a Majorana qubit in a quantum dot-superconductor array. *Phys. Rev. B* **111**, 075416 (2025).

Methods

Fabrication and yield

All devices were fabricated using the techniques described in detail in ref. 49 (Q.W., manuscript in preparation). Aluminium loop structures (Q.W., manuscript in preparation) are defined in an InSbAs-Al chip by wet etching, followed by the deposition of three ohmic Ti/Pd contacts. After deposition of 20 nm AlO_x by 40 °C atomic layer deposition (ALD), three large Ti/Pd depletion gates are evaporated: one large top depletion gate and two bottom depletion gates, each extending halfway. The bottom consists of two gates to independently form the left and right halves of the channel, separated by a thin channel in which the middle lead is placed. This simplifies placing an additional gate in front of the middle ohmic contact, to have a well-defined tunnelling barrier for the middle probe. Moreover, it simplifies finding a suitable active region in which the 2DEG is depleted below the gates, whereas a narrow conductance channel remains in between. The channel width is designed to be 200 nm. Following a second ALD layer (20 nm AlO_x), a first layer of six Ti/Pd finger gates is evaporated. These are used for controlling the electrochemical potential energies of the QDs and hybrid regions and for defining the tunnelling barrier for the middle contact. A third ALD layer (20 nm AlO_x) is deposited, followed by evaporation of the remaining six Ti/Pd finger gates that define the three QDs. For radiofrequency measurements, superconducting LC-resonator circuits are fabricated on a separate chip with a silicon substrate, by etching NbTiN. To apply d.c. voltages, bias tees are created by depositing 20 nm Cr structures with resistances of around 5 kΩ.

For the investigation presented in this paper, 16 devices were fabricated, with small variations in device dimensions. Of these, 12 had no visible defects under optical/SEM inspection of the finished devices. We faced some challenges in simultaneously connecting all 15 gates to the printed circuit board and connecting all three ohmic contacts through the resonator chip. In total, six devices were bonded and cooled down, of which in five instances, fridge wiring and bonding issues caused gate or ohmic connections to be absent once reaching millikelvin temperatures. Once these issues were resolved, the final device was used for obtaining the measurements demonstrated in this paper. This device was cooled down twice over the course of 5 months, in which we were able to reproduce our findings when restarting from a 'reset' device. The main text highlights results within a single cooldown; data from the other sets of experiments are included here.

Transport measurements

Measurements are performed in a dilution refrigerator with a base temperature of 20 mK. Transport measurements presented in the main text are performed in a.c. and d.c. using a four-terminal set-up (three ohmic contacts plus two aluminium strips connected in a loop). The aluminium strips induce a gap of about 220 μV (Extended Data Fig. 1) and are kept electrically grounded. Each ohmic lead is connected to a current meter and biased through a digital-to-analog converter, and both d.c. and a.c. voltages can be applied. Offsets of the applied voltage bias on each lead are corrected by independently measuring the Coulomb peaks in the QDs and looking at the change in sign of the current. The voltage outputs of the current meters are recorded with three digital multimeters and three lock-in amplifiers. When applying a d.c. voltage to one lead (for example, V_L), the other leads (that is, V_M and V_R) are kept grounded. The a.c. excitations are applied with amplitudes around 5 μV RMS and a frequency of 23 Hz. In this way, a full conductance matrix $G_{ij} = \frac{dI_i}{dV_j}$ is obtained by measuring the response of I_L, I_M and I_R, to V_L, V_M and V_R. Three separate measurements are required, as only a single lead is biased at a time. Small offsets in measured conductances arise using the lock-in amplifiers because of capacitances to ground within the electronics. These offsets are calibrated using Coulomb blockaded measurements and corrected. It should be noted that voltage-divider effects arise when applying biases in a four-terminal set-up. For three-terminal set-ups, the measured conductances and applied biases are generally corrected[50]. For a four-terminal set-up, however, this calculation gets cumbersome. Here, we focus on low tunnelling regimes ($G \ll 2e^2/h$), in which the device resistance is large compared with the resistances of the fridge lines and the current meters, such that the multi-terminal effect is small. Nevertheless, this should be kept in mind when, for example, interpreting the non-local conductances in Extended Data Fig. 9.

Magnetic fields are applied using a three-dimensional vector magnet. The field perpendicular to the superconducting loop (B_z) is generated using a high-resolution current source, giving a B_z resolution below 0.1 μT (providing sufficient resolution for the flux period of 28 μT). A small (but significant) hysteresis of the order of 5 μT is observed when sweeping B_z in opposite directions. This is counteracted by setting B_z first to −100 μT and then sweeping this field back in the positive direction, such that consecutive experiments where B_z is varied are consistent. To perform spin polarization of the QDs, a magnetic field of 200 mT is applied parallel to the channel (B_x). Owing to an imperfection in the alignment, this introduces a small B_z component as well, of the order of 80 flux quanta. It was not possible to accurately correct this offset for this work, and so we do not determine the B_x value that corresponds to precisely 0 flux through the loop.

Radiofrequency-reflectometry measurements

The experiments require the tuning of 15 gate voltages to create the three-site chain, which results in a large parameter space of gate voltages. To speed up the tuning process, we use radiofrequency lead reflectometry[51], in addition to the d.c. conductance measurements. Each ohmic contact is connected to an inductor, designed with varying inductances $L_L = 0.2$ Hz, $L_M = 0.5$ Hz and $L_R = 1.5$ μH, that together with a parasitic capacitance to ground by bond-wires result in resonators with frequencies of $f_L = 723$ Hz, $f_M = 505$ Hz and $f_R = 248$ MHz. A complete circuit diagram, including the fridge wiring and filters, is provided in ref. 52. Using a directional coupler, we obtain the reflected signal of each lead. We denote the normalized reflected signals of the left, middle and right lead as S_{21}^L, S_{21}^M and S_{21}^R, respectively, which correspond roughly linearly to conductance. All three signals can be measured simultaneously through multiplexing[53], using the circuit shown in Extended Data Fig. 1. In combination with saw-tooth pulses on the QD plunger gates, generated by arbitrary waveform generators, this allows for scanning the parameter space many times faster than through d.c. measurements. For clarity, throughout the extended data figures, the data obtained with RF reflectometry are shown in a different colour map from the d.c. conductance data.

Device tune-up

Here, we detail how the device was tuned to reach the point of obtaining the measurements presented in the main text. To start, a conductance channel has to be isolated by tuning the three large depletion gates. A regime is obtained in which the 2DEG is fully depleted below these gates, but a finite current remains in the channel. Next, we perform tunnel spectroscopy of the hybrid regions to verify the presence of gate-tunable sub-gap states (Extended Data Fig. 1). Then, the remaining gates are activated to form the three QDs. We find a regime in which the QDs are stable and contain orbitals with a large level spacing, such that sufficient Zeeman energies can be induced through the external magnetic field without mixing states in neighbouring orbitals. The InSbAs heterostructure investigated in this paper does not have a capping layer, such that the confinement layer is very close to the surface[49]. Thus, the QDs can couple easily to disorder in the dielectric, resulting in regimes in parameter space that are unstable. This constitutes a challenge in tuning up all three QDs into stable regimes (Extended Data Fig. 3). Once such a stable regime is found, we tune the interdot couplings by studying CSDs of the QDs and the ABSs in the hybrid regions, following the protocols in refs. 34,36. An important

requirement is that the interdot coupling amplitudes should exceed the line width of the conductance measurements, to resolve the full density of states. However, if the middle QD is too strongly coupled to both hybrids, its chemical potential energy becomes dependent on the superconducting phase[54]. In this case, the interdot coupling amplitudes (t,Δ) themselves become phase dependent and additional modulations in the conductance spectra are observed (Extended Data Fig. 5e). We limited the coupling between the ABSs and the middle QD to stay away from this regime (as verified by Extended Data Fig. 4d,h), to compare the conductance spectra as a function of B_z directly to the Kitaev chain model in Fig. 2. For the conductance spectra measurements shown in Figs. 2 and 3, it is crucial that the QDs remain on resonance throughout the measurements. The centre of each resonance was determined by measuring independently the Coulomb resonances for each QD in radiofrequency reflectometry and fitting a Lorentzian line shape. This was done directly before and after each measurement to verify that no gate jump or drift occurred. Moreover, CSDs for the left and right QD pairs were obtained before and after each set of measurements, to ensure that the interdot couplings had not changed. In case any gate-jumps occurred, the measurements were repeated.

Kitaev model and numerical calculations of conductance

The Hamiltonian of a three-site Kitaev chain is given by

$$H=\mu_1 n_1+\mu_2 n_2+\mu_3 n_3+(t_1 c_2^{\dagger}c_1+t_2 c_3^{\dagger}c_2+\Delta_1 c_2 c_1+\Delta_2 e^{i\phi_\Delta}c_3 c_2+\text{h.c.}), \quad (1)$$

where c_i is the annihilation operator for the fermion on the ith site, $n_i=c_i^{\dagger}c_i$ is the number operator, μ_i is the on-site energy, t_i and Δ_i are the normal and superconducting tunnelling amplitudes between neighbouring sites, and ϕ_Δ is the phase difference between the two superconducting leads, which can be controlled by the magnetic flux threading through the loop. The corresponding Bogoliubov–de Gennes Hamiltonian is

$$h_{K3}=\begin{pmatrix} \mu_1 & t_1 & 0 & 0 & \Delta_1 & 0 \\ t_1 & \mu_2 & t_2 & -\Delta_1 & 0 & \Delta_2 e^{-i\phi_\Delta} \\ 0 & t_2 & \mu_3 & 0 & -\Delta_2 e^{-i\phi_\Delta} & 0 \\ 0 & -\Delta_1 & 0 & -\mu_1 & -t_1 & 0 \\ \Delta_1 & 0 & -\Delta_2 e^{i\phi_\Delta} & -t_1 & -\mu_2 & -t_2 \\ 0 & \Delta_2 e^{i\phi_\Delta} & 0 & 0 & -t_2 & -\mu_3 \end{pmatrix} \quad (2)$$

in the basis of $(c_1^{\dagger}, c_2^{\dagger}, c_3^{\dagger}, c_1, c_2, c_3)$. To calculate the differential conductance through the system, we use the scattering matrix method, where the S matrix can be obtained from the Weidenmuller formula as below

$$S(\omega)=\begin{pmatrix} S^{\text{ee}} & S^{\text{eh}} \\ S^{\text{he}} & S^{\text{hh}} \end{pmatrix}=\hat{1}-iW^{\dagger}\left(\omega-h_{K3}+\frac{i}{2}WW^{\dagger}\right)^{-1}W, \quad (3)$$

where $W=$ diag $(\sqrt{\Gamma_1}, \sqrt{\Gamma_2}, \ldots, -\sqrt{\Gamma_1}, -\sqrt{\Gamma_2}, \ldots)$ is the matrix describing the dot–lead couplings, with Γ_i being the coupling strength between dot i and lead i. The zero-temperature conductance is thus

$$G_{\alpha\beta}^{(0)}(\omega)=\delta_{\alpha\beta}-\left|S_{\alpha\beta}^{\text{ee}}(\omega)\right|^2+\left|S_{\alpha\beta}^{\text{he}}(\omega)\right|^2 \quad (4)$$

in units of e^2/h. The finite-temperature conductance is obtained by a convolution between the zero-temperature conductance and the derivative of the Fermi distribution

$$G_{\alpha\beta}^{T}(\omega)=\int_{-\infty}^{+\infty} dE \frac{G_{\alpha\beta}^{(0)}(E)}{4k_B T\cosh^2[(E-\omega)/2k_B T]}. \quad (5)$$

In the numerical calculations shown in the current work, we use $t_1=\Delta_1=20$ μeV, $t_2=\Delta_2=25$ μeV, which are extracted from experimental data in Fig. 1. Moreover, we set $\Gamma_1=\Gamma_2=\Gamma_3=0.7$ μeV, which does not affect the simulations qualitatively, but were selected to give the same order of magnitude of conductance. Finally, we set $T=50$ mK.

The Kitaev chain in the Majorana basis

To guide the interpretation of the measurements, it is instructive to consider the three-site Kitaev chain Hamiltonian in terms of Majorana operators. This is done by introducing two Majorana operators for each fermionic site:

$$c_n=(\gamma_{na}+i\gamma_{nb})/\sqrt{2}, \quad c_n^{\dagger}=(\gamma_{na}-i\gamma_{nb})/\sqrt{2}, \quad \{\gamma_{ma},\gamma_{nb}\}=\delta_{mn}\delta_{ab}. \quad (6)$$

As such, the Hamiltonian can be written as

$$\begin{aligned} H=&\,i\mu_1\gamma_{1a}\gamma_{1b}+i\mu_2\gamma_{2a}\gamma_{2b}+i\mu_3\gamma_{3a}\gamma_{3b}+i(t_1+\Delta_1)\gamma_{2a}\gamma_{1b} \\ &+i(-t_1+\Delta_1)\gamma_{2b}\gamma_{1a}+it_2\gamma_{3a}\gamma_{2b}-it_2\gamma_{3b}\gamma_{2a} \\ &+i\Delta_2\cos\phi(\gamma_{3a}\gamma_{2b}+\gamma_{3b}\gamma_{2a})+i\Delta_2\sin\phi(\gamma_{3a}\gamma_{2a}-\gamma_{3b}\gamma_{2b}). \end{aligned} \quad (7)$$

Therefore, at the sweet spot of a three-site Kitaev chain, that is, $\mu_n=0$, $t_1=\Delta_1$, $t_2=\Delta_2$, $\phi=0$, we have

$$H(\phi=0)=i2t_1\gamma_{2a}\gamma_{1b}+i2t_2\gamma_{3a}\gamma_{2b}. \quad (8)$$

By contrast, at $\mu_n=0$, $t_1=\Delta_1$, $t_2=\Delta_2$, $\phi=\pi$, the Hamiltonian becomes

$$H(\phi=\pi)=i2t_1\gamma_{2a}\gamma_{1b}-i2t_2\gamma_{3b}\gamma_{2a}. \quad (9)$$

A bilinear term of Majorana operators indicates a coupling between them. This is what is visualized through the schematics used in Fig. 2c.

Majorana zero modes for a Kitaev chain at $\phi=0$ and $\phi=\pi$

We now calculate the wavefunctions of Majorana zero modes of the Kitaev chain. To distinguish it from the Majorana basis using γs, we use χ_n to denote the Majorana zero modes. The definition of a Majorana zero-energy quasiparticle is

$$[H,\chi_n]=0, \quad \chi_n^{\dagger}=\chi_n. \quad (10)$$

For the Kitaev chain with $\phi=0$, the solutions are easily obtained: as γ_{1a} and γ_{3b} do not appear in the Hamiltonian in equation (8), the wavefunctions of the two Majorana zero modes are

$$\chi_1=\gamma_{1a}, \quad \chi_2=\gamma_{3b}, \quad (11)$$

that is, one is completely localized at the left QD and the other at the right QD, separated in space by the middle QD. By contrast, when $\phi=\pi$, there exist four Majorana zero modes, of which the first three are again easy to find as shown below:

$$\chi_1=\gamma_{1a}, \quad \chi_2=\gamma_{2b}, \quad \chi_3=\gamma_{3a}. \quad (12)$$

They are localized at the left, middle and right QD, respectively. The ansatz of the fourth Majorana zero mode is $\chi_4=A\gamma_{1b}+B\gamma_{2a}+C\gamma_{3b}$, which yields

$$\chi_4=\frac{t_2}{\sqrt{t_1^2+t_2^2}}\gamma_{1b}-\frac{t_1}{\sqrt{t_1^2+t_2^2}}\gamma_{3b}. \quad (13)$$

That is, χ_4 is delocalized at the left and right QDs (no wavefunction weight in the middle dot), with the relative weights determined by the gap of the left and right pairs. We can note that once the left or right QD is detuned from resonance, that is, a finite μ_1 or μ_3, χ_4 would couple with χ_1 or χ_3, giving an energy splitting. This explains the splitting of the zero-bias conductance peak observed in the π-phase Kitaev chain studied in the main text (Fig. 3d).

The Majorana density

The main text focuses on conductance spectra of the three-site Kitaev chain at $\phi_\Delta = 0$, when the left QD is detuned. Here we show that an isolated zero-bias conductance peak reveals the Majorana wavefunction profiles. Assuming equal dot–lead coupling strengths $\Gamma_i = \Gamma$ and an isolated zero-energy state of h_{K3}, the S matrix can be simplified to

$$S(\omega) \approx \hat{1} - \mathrm{i}\frac{\Gamma}{\omega + \mathrm{i}\frac{\Gamma}{2}} \begin{pmatrix} u_1 u_1^* + v_1^* v_1, \ldots \\ u_2 u_1^* + v_2^* v_1, \ldots \\ \vdots \\ -(v_1 u_1^* + u_1^* v_1), \ldots \\ -(v_2 u_1^* + u_2^* v_1), \ldots \\ \vdots \end{pmatrix}, \tag{14}$$

where u_i and v_i are the electron and hole components of the zero-energy quasiparticle state on-site i. By definition $u^* = (\xi_A + \mathrm{i}\xi_B)/\sqrt{2}$, $v = (\xi_A - \mathrm{i}\xi_B)/\sqrt{2}$, where ξ_A and ξ_B are Majorana wavefunctions. We thus have $uu^* + v^*v = |\xi_A|^2 + |\xi_B|^2$, $-2u^*v = -(\xi_A^2 + \xi_B^2)$. Furthermore, h_{K3} is real at $\phi = 0$, giving real u and v. Thereby ξ_A is purely real and ξ_B is purely imaginary, giving $uu^* + v^*v = \rho_A + \rho_B$, $-2u^*v = -(\rho_A - \rho_B)$, where $\rho_{A/B} = |\xi_{A/B}|^2$ are the local Majorana densities. As a result, the local conductance in the zero-temperature limit is

$$G_{ii}^{(0)}(\omega) = \frac{(\Gamma/2)^2}{\omega^2 + (\Gamma/2)^2} \cdot 4(\rho_{\mathrm{A}i} + \rho_{\mathrm{B}i} - 4\rho_{\mathrm{A}i}\rho_{\mathrm{B}i}). \tag{15}$$

Here, the profile of the zero-bias conductance peak has a Lorentzian shape with its broadening width being fixed by the dot–lead coupling strength. Although finite-temperature effects will change this prefactor, a key finding here is that the local zero-bias conductance of a multi-terminal junction is proportional to the Majorana densities.

For a three-site Kitaev chain at its sweet spot, as considered in the current work, the zero-energy eigenfunction is $\psi = \frac{1}{2}\left(\frac{1}{\sqrt{1+4a^2}}, \frac{-2a}{\sqrt{1+4a^2}}, 1, \frac{-1}{\sqrt{1+4a^2}}, \frac{2a}{\sqrt{1+4a^2}}, 1\right)^{\mathrm{T}}$, giving $\rho_A = (0, 0, 1/2)$ and $\rho_B = \frac{1}{2}\left(\frac{1}{1+4a^2}, \frac{4a^2}{1+4a^2}, 0\right)$ where $a = \mu_1/4t$ is the dot detuning with respect to the gap. Therefore, the profiles of local zero-bias conductances as a function of dot detuning are

$$\begin{aligned} G_{11}(V=0) &\propto 2\rho_B = \frac{1}{1+4a^2}, \\ G_{22}(V=0) &\propto 2\rho_B = \frac{4a^2}{1+4a^2}, \\ G_{33}(V=0) &\propto 2\rho_A = 1. \end{aligned} \tag{16}$$

Thus, the local conductance profiles as a function of dot detuning indicate the moving of Majorana zero modes in a three-site chain. We compare these findings with the experimental data in Extended Data Fig. 8.

Line shape of conductance traces

When probing the excitation gap in the middle QD at the three-site sweet spot (Fig. 2), a finite in-gap conductance remains. In part, this can be expected because of thermal-broadening effects on the higher-energy excitations. We address here the expected line shapes for the conductances at a three-site sweet spot. The conductance measurements are performed in the limit of low tunnelling between the leads and the QDs, such that we can expect the QD–lead coupling $\Gamma \ll k_{\mathrm{B}}T$. In this limit, the line shape of a single QD resonance as a function of applied V_{bias} is given by[55]

$$G(V_{\mathrm{bias}}) \propto A \cosh\left(\frac{V_{\mathrm{bias}}}{2k_{\mathrm{B}}T}\right)^{-2}. \tag{17}$$

In conductance measurements of a three-site chain sweet spot, the density of states depends on the site that is probed. For the left QD, three conductance peaks are expected: one at zero bias, and two at $\pm 2t_1$. We thus model the conductance G_{LL} as a function of V_{L} to be the sum of three contributions:

$$\begin{aligned} G_{\mathrm{LL}}(V_{\mathrm{L}}) = A_1 \cosh\left(\frac{V_{\mathrm{L}} - 2t_1}{\gamma}\right)^{-2} + A_2 \cosh\left(\frac{V_{\mathrm{L}}}{\gamma}\right)^{-2} \\ + A_3 \cosh\left(\frac{V_{\mathrm{L}} + 2t_1}{\gamma}\right)^{-2}, \end{aligned} \tag{18}$$

where we replace the factor of $2k_{\mathrm{B}}T$ with a general broadening factor γ. Similarly, the right QD has three conductance peaks: one at zero bias, and two at $\pm 2t_2$. We model the conductance G_{RR} as a function of V_{R} to be

$$\begin{aligned} G_{\mathrm{RR}}(V_{\mathrm{R}}) = B_1 \cosh\left(\frac{V_{\mathrm{R}} - 2t_2}{\gamma}\right)^{-2} + B_2 \cosh\left(\frac{V_{\mathrm{R}}}{\gamma}\right)^{-2} \\ + B_3 \cosh\left(\frac{V_{\mathrm{R}} + 2t_2}{\gamma}\right)^{-2}. \end{aligned} \tag{19}$$

From these fits, the values of t_1 and t_2 are determined. The conductance of the middle QD is then expected to have four peaks: at $\pm t_1$ and at $\pm t_2$, giving the sum of the following four contributions:

$$\begin{aligned} G_{\mathrm{MM}}(V_{\mathrm{M}}) = C_1 \cosh\left(\frac{V_{\mathrm{M}} - 2t_1}{\gamma}\right)^{-2} + C_2 \cosh\left(\frac{V_{\mathrm{M}} + 2t_1}{\gamma}\right)^{-2} \\ + C_3 \cosh\left(\frac{V_{\mathrm{M}} - 2t_2}{\gamma}\right)^{-2} + C_4 \cosh\left(\frac{V_{\mathrm{M}} + 2t_2}{\gamma}\right)^{-2}. \end{aligned} \tag{20}$$

These analytical expressions are in close agreement with the conductance traces obtained from the numerical simulations, in the parameter regime described above. We compare the expressions to experimental data in Extended Data Fig. 5.

Data availability

All raw data obtained in this study and the scripts to produce the figures are available at Zenodo[56].

49. Moehle, C. M. et al. InSbAs two-dimensional electron gases as a platform for topological superconductivity. *Nano Lett.* **21**, 9990–9996 (2021).
50. Martinez, E.A. et al. Measurement circuit effects in three-terminal electrical transport measurements. Preprint at arxiv.org/abs/2104.02671 (2021).
51. Vigneau, F. et al. Probing quantum devices with radio-frequency reflectometry. *Appl. Phys. Rev.* **10**, 021305 (2023).
52. Kulesh, I. et al. A flux-controlled two-site Kitaev chain. Preprint at arxiv.org/abs/2501.15912 (2025).
53. Hornibrook, J. M. et al. Frequency multiplexing for readout of spin qubits. *Appl. Phys. Lett.* **104**, 103108 (2014).
54. Pavešič, L., Aguado, R. & Žitko, R. Strong-coupling theory of quantum-dot Josephson junctions: Role of a residual quasiparticle. *Phys. Rev. B* **109**, 125131 (2024).
55. Beenakker, C. W. J. Theory of Coulomb-blockade oscillations in the conductance of a quantum dot. *Phys. Rev. B* **44**, 1646–1656 (1991).
56. Haaf, S. L. D. Data and code for "Edge and bulk states in a three-site Kitaev chain". *Zenodo* https://doi.org/10.5281/zenodo.15020006 (2025).
57. Jellinggaard, A., Grove-Rasmussen, K., Madsen, M. H. & Nygård, J. Tuning Yu-Shiba-Rusinov states in a quantum dot. *Phys. Rev. B* **94**, 064520 (2016).

Acknowledgements We thank O. W. B. Benningshof and J. D. Mensingh for technical assistance with the cryogenic electronics. We thank L. Vandersypen, R. Aguado, R. Seoane, M. Leijnse, G. Wang, A. M. Bozkurt, N. van Loo, G. P. Mazur, F. Zatelli and L. Kouwenhoven for providing valuable inputs on the paper. The research at Delft was supported by the Dutch National Science Foundation (NWO), Microsoft Corporation Station Q and a grant from the Top Consortium for Knowledge and Innovation (TKI) program. S.G. and M.W. acknowledge financial support from the Horizon Europe Framework Program of the European Commission through the European Innovation Council Pathfinder grant no. 101115315 (QuKiT).

Author contributions Q.W. fabricated the device, with input from S.L.D.t.H and I.K.; Y.Z. and I.K. fabricated the resonator circuits. C.G.P. and I.K. designed the measurement set-up. Measurements were performed by S.L.D.t.H, V.P.M.S., Y.Z. and A.B.; C.-X.L. and M.W. provided

the theoretical analysis, with C.-X.L. carrying out the analytical calculations and the numerical simulations. MBE growth of the semiconductor heterostructures and the characterization of the materials were performed by D.X. and C.T. under the supervision of M.J.M. The paper was written by S.L.D.t.H. and S.G., with input from all co-authors. S.G. supervised the experimental work in Delft.

Competing interests The authors declare no competing interests.

Additional information

Supplementary information The online version contains supplementary material available at https://doi.org/10.1038/s41586-025-08892-5.

Correspondence and requests for materials should be addressed to Srijit Goswami.

Peer review information *Nature* thanks the anonymous reviewers for their contribution to the peer review of this work. Peer reviewer reports are available.

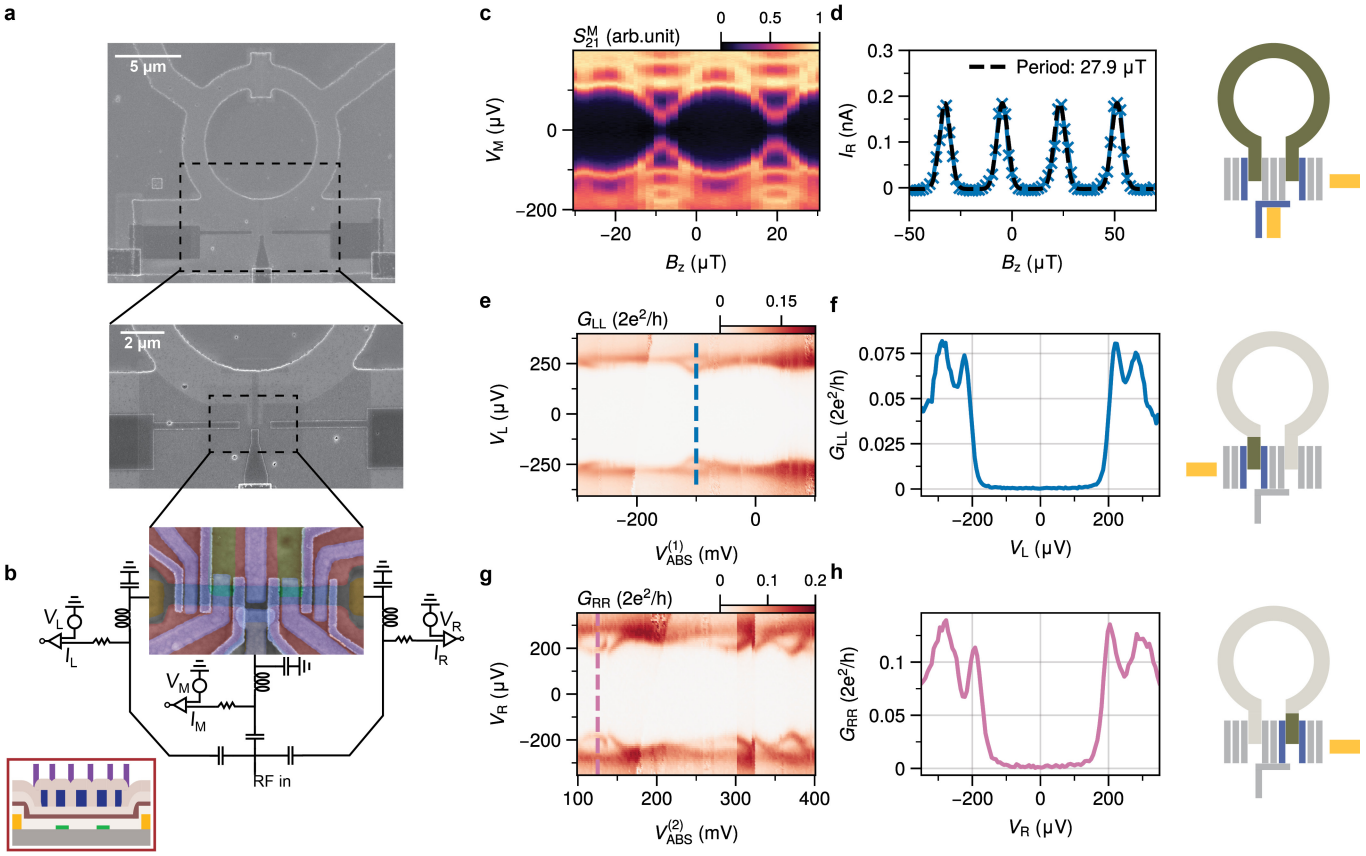

Extended Data Fig. 1 | Device description and characterisation of hybrid sections. a. Zoomed out SEMs of copies of the measured device obtained after deposition of Ohmic contacts, showing the full structure of the superconducting loop. **b**. Close-up SEM of the finished device, including the full circuit diagram. Bottom left in-set shows a cross-sectional schematic of the device along the channel, adapted from Q.W. (manuscript in preparation), to visualise the order of the three gate layers. Resonators are formed by inductors in combination with a parasitic capacitances to ground, which allows for fast radio-frequency (RF) measurements, used in this work for tuning and characterisation of the system. Voltage sources and current meters are attached to each lead via ≈ 5 kΩ resistors, acting as bias tees, used to obtain the conductance measurements in the main text. Sub-figures (c-h.) show characterisations of the three possible hybrid configurations, after a 1-D channel is formed with the large depletion gates. Schematics on the right display the activated tunneling gates and relevant Ohmic contacts for each row. **c**. RF-spectroscopy of the Josephson junction formed by the two superconducting fingers at the ends of the loop, as a function of the magnetic field B_z perpendicular to the loop. **d** Measured current I_R with $V_R = 100\,\mu V$, in a wider range of B_z. Fitting the oscillations with a periodic Gaussian function provides an estimate for the flux periodicity (28 µT). **e** Tunneling spectroscopy of the left SC finger in isolation, as a function of $V_{ABS}^{(1)}$ applied to the gate covering the left hybrid region. **f**. Line-trace from (e) at $V_{ABS}^{(1)} = -100$ mV, to show the presence of a sub-gap state in the left hybrid. **g**. Tunneling spectroscopy of the right SC finger in isolation, as a function of the gate covering the right hybrid region ($V_{ABS}^{(2)}$). **h**. Line-trace from (g) at $V_{ABS}^{(2)} = 125$ mV to show the presence of a sub-gap state in the right hybrid.

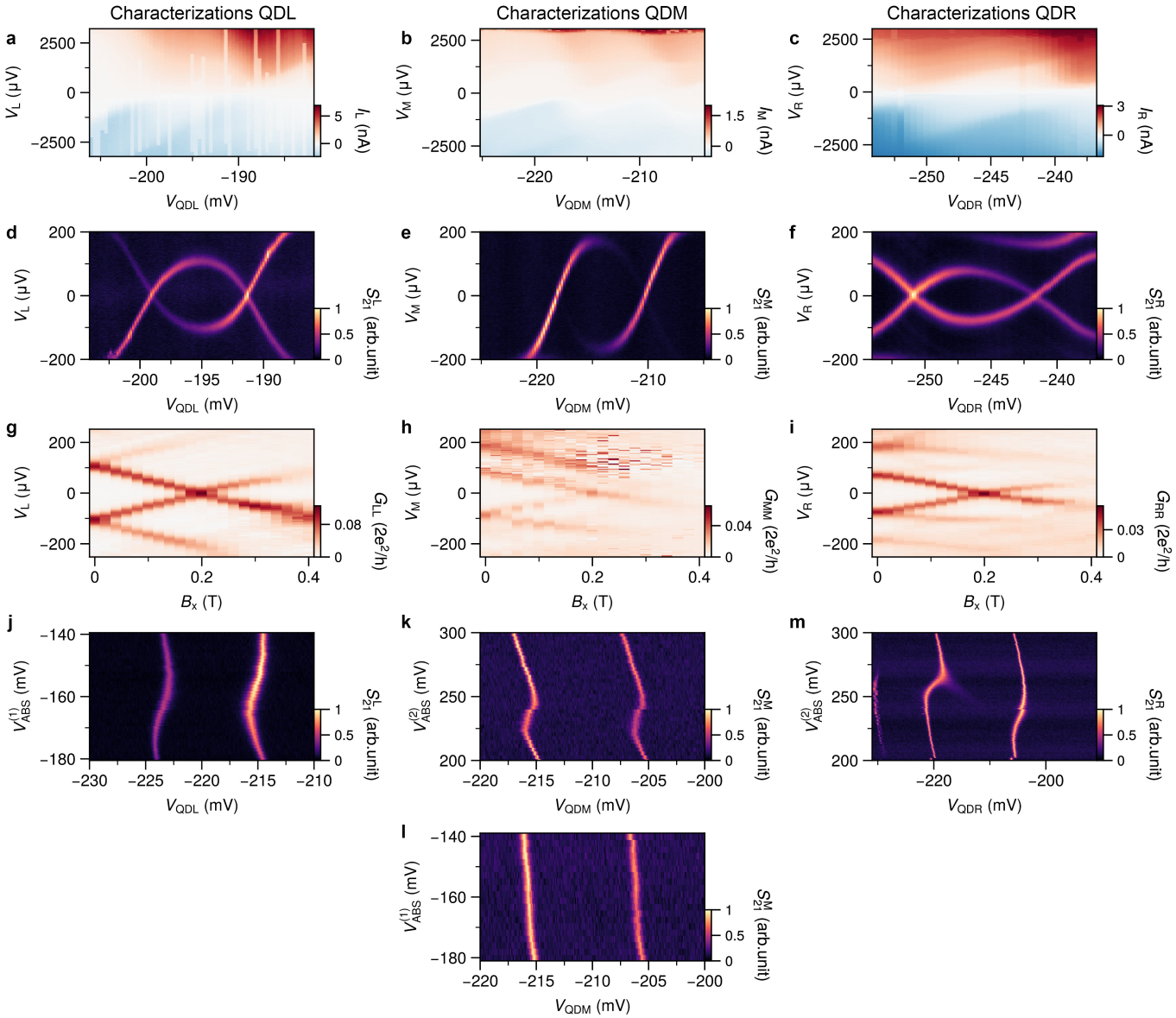

Extended Data Fig. 2 | Quantum dot characterisations. Results presented in the main text are obtained using a single orbital in each QD. Characterisation measurements of each QD is shown here. Left, middle and right columns pertain to the left, middle and right QD respectively. **a-c**. Coulomb diamonds measured at $B_x = 0$ mT. To achieve strong interdot coupling, barriers between QD and neighbouring regions are kept relatively open, such that a finite current can be observed within each Coulomb diamond. The outline roughly indicates the charging energies to be > 1 mV. **d-f**. RF-Spectroscopy of each QD in the same regime as (a-c), for a smaller range of applied voltage biases. In this strong coupling regime, so-called Yu-Shiba-Rusinov states form at sub-SC gap energy scales whose energies are non-linearly dependent on the plunger gate voltages[57]. **g-i**. Spectroscopy as a function of magnetic field B_x applied along the 1-D channel, with each plunger gate set close to the zero field charge degeneracy point based on (d-f). The slope of the splitting sub-gap states provides an estimate of the *g*-factors for these parameters to be 18.4, 14.8 and 13.7 respectively. **j-m**. Examples of QD-ABS charge stability diagrams, used to calibrate the interdot interactions following the procedure detailed in[34,36]. The discrepancies in the plunger gate voltages used for each orbital between (a-c) and (j-m) arise due to gate-jumps and cross-talk between neighbouring barrier gates.

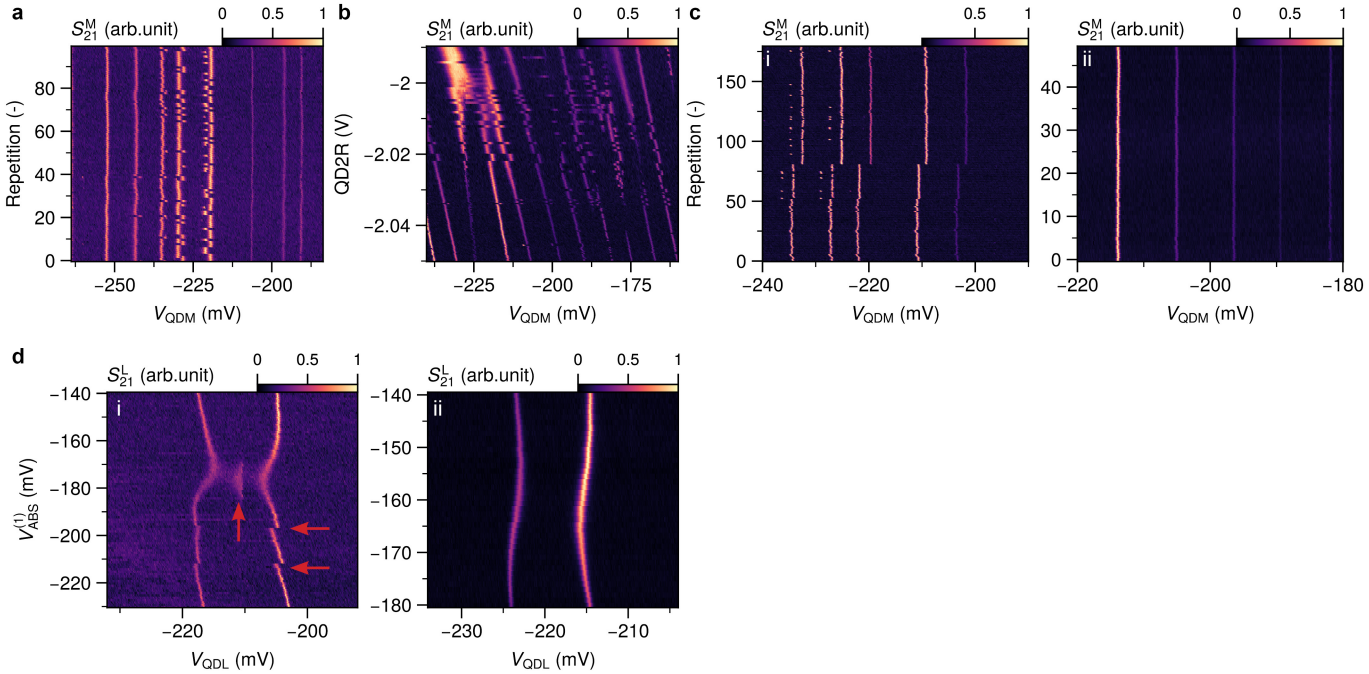

Extended Data Fig. 3 | QD stability. a. Example of repeated RF-measurements of the middle QD resonances. The same measurement was repeated 100 times, once every second. The plot shows a stack of all repetitions. The resonances at −225 mV are observed to switch between two states during this time, which makes them unsuitable for slow DC measurements. **b**. In order to find a stable regime, we observe the effect of varying the barrier gates forming the QDs. Here, for example, the middle QD resonances are found to be more stable when the right barrier gate is tuned below −2.02 V. **c**. This becomes apparent when comparing repeated RF measurements for (i) unstable and (ii) stable regimes. **d**. In addition, charge-jumps in the gate voltages can affect the charge-stability diagrams. Panel (i) shows an example of a CSD for QDL and the left hybrid gate, where charge jumps occur in both V_{ABS}^{1} and V_{QDL} (indicated by the red arrows). By fine-tuning the barrier gates forming QDL, we can reach a state where these jumps are avoided in the region of interest, shown in panel (ii).

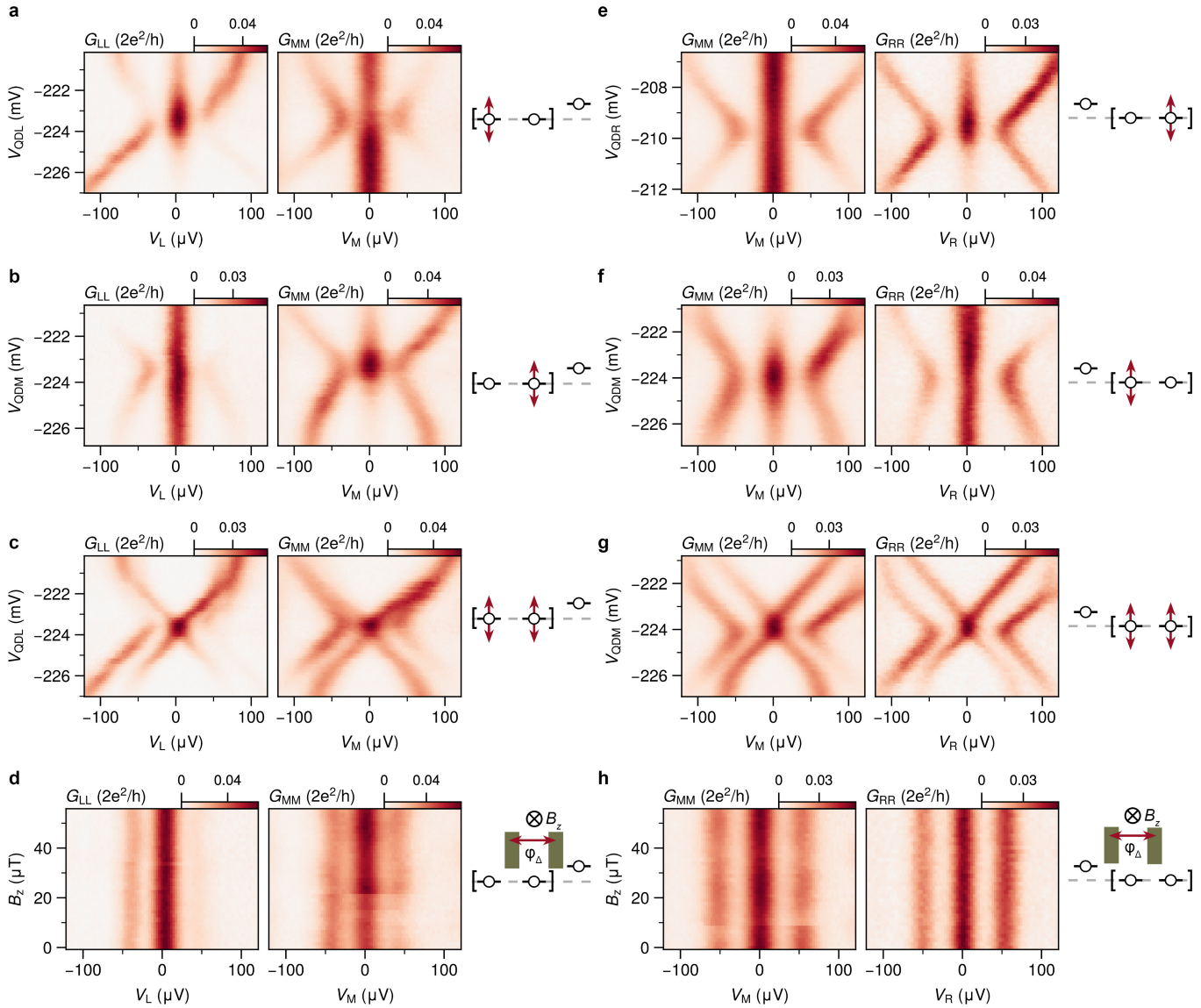

Extended Data Fig. 4 | Conductance spectra of two-site QD pairs. Studying CSDs for pairs of QDs provides information about the interdot couplings and allows one to reach the sweet spot conditions shown in Fig. 1c,d. In addition, finite bias conductance spectra at the two-site sweet spots should be obtained[35] for all possible combinations of QD detunings. This is shown here for the charge configuration in Fig. 1. Adjacent schematics represent the configurations of the QDs and the parameters varied. Left column: tunneling spectroscopies of the left QD pair at a sweet spot (i.e. $t_1 = \Delta_1$), with the right QD kept in Coulomb blockade. G_{LL} and G_{MM} are measured as a function of **a**. detuning V_{QDL}, **b**. detuning V_{QDM}, **c**. detuning both V_{QDL} and V_{QDM} simultaneously and **d**. Applying a magnetic field B_z perpendicular to the superconducting loop. Right column: tunneling spectroscopy of the right pair of QDs at a sweet spot (i.e. $t_2 = \Delta_2$), with the left QD kept in Coulomb blockade. G_{MM} and G_{RR} are measured as a function of **e**. detuning V_{QDR} **f**. detuning V_{QDM}, **g**. detuning both V_{QDM} and V_{QDR} and **h**. Applying a magnetic field B_z perpendicular to the superconducting loop. It is important to note that (d) and (h) are obtained for the same configuration as the flux-dependence measurements in Fig. 2, with the only difference being that here the outer QD is kept in Coulomb blockade. The lack of response to B_z rules out more trivial origins of the flux dependence in Fig. 2, such as oscillations of the middle QDs electrochemical potential energy.

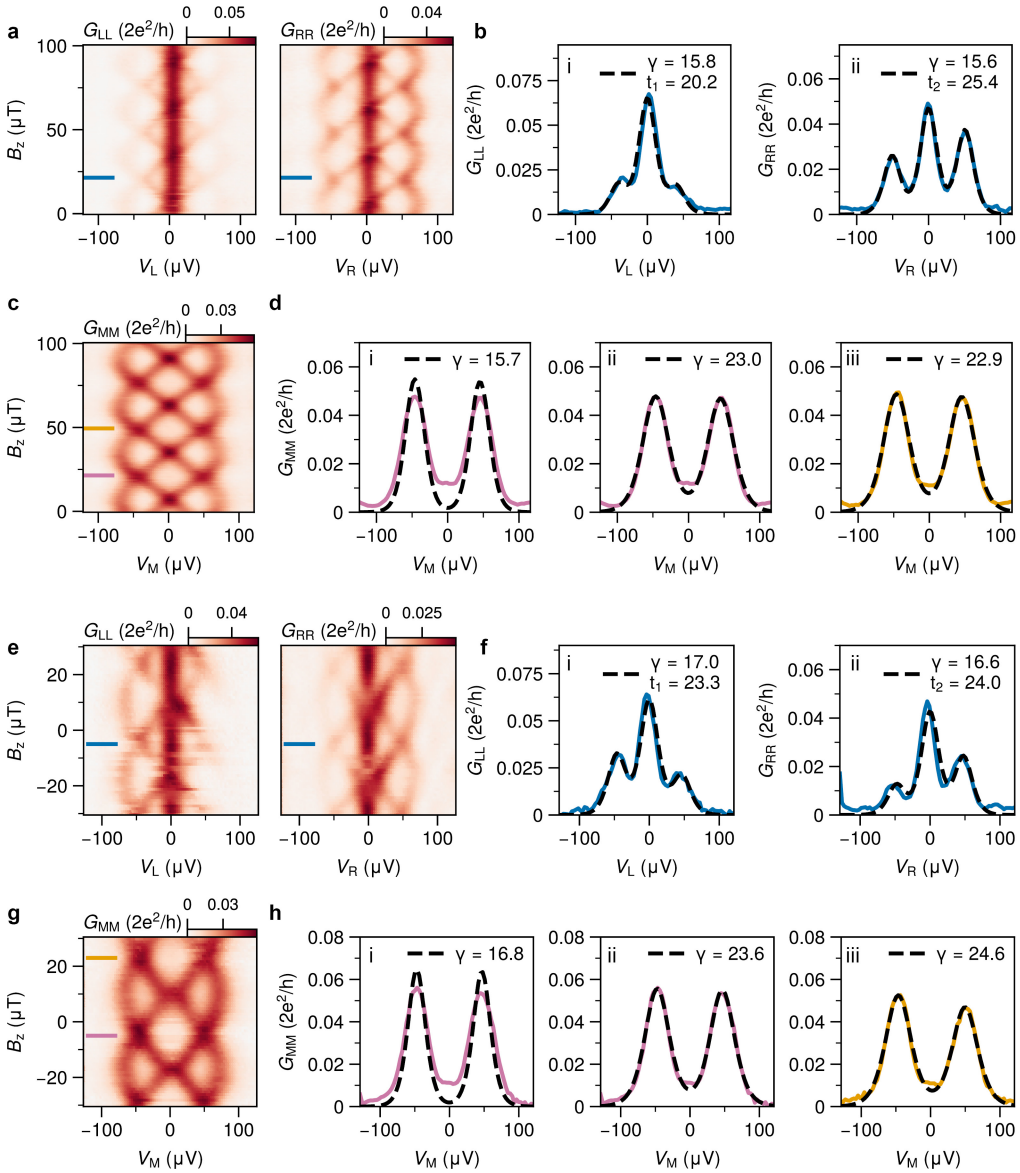

Extended Data Fig. 5 | Fitting of conductance line-traces. The measurements in Fig. 2 show a finite in-gap conductance in G_{MM} when $\phi_\Delta = 0$. Possible origins for this include thermal broadening, and small deviations in the QD plunger gate voltages from being precisely at $\mu_i = 0$. Here we address the former, by comparing the conductance bias-traces with the theoretically expected shapes in the small lead-QD coupling limit ($\Gamma \ll k_B T$) described in Methods. **a**. Repetitions of conductance spectra for G_{LL} and G_{RR} as a function of B_z, as shown in Fig. 2a. **b**. Line-cuts taken from the indicated position in (a), at B_z corresponding to $\phi_\Delta = 0$. G_{LL} is fitted to Eq. (18) and G_{RR} is fitted to Eq. (19), yielding estimates for t_1 and t_2. We find the conductances are well described by the temperature-limited fits and find both are described by the same broadening parameter ($\gamma = 15.6$). **c**. Repetition of conductance spectra for G_{MM} as a function of B_z from Fig. 2a. **d**. Using the t_1 and t_2 values extracted in (b), we fit the indicated G_{MM} line-cut from (c) to Eq. (20). In (i), γ is fixed to be the same value as extracted in (b), while in (ii) γ is included as fitting parameter. (iii) uses the same fitting as (ii), for a line-cut taken at a different 2π period as indicated in (c). The conductance is again well-described by the temperature-limited fit. A larger broadening parameter is however required, the origin of which is unclear and not captured by the numerical simulations. In (ii) and (iii) the measured conductance at $V_M = 0$ is $\approx 3\ mG_0$ larger than explained by the fits. From Eq. (16), this remainder would correspond to offsets in μ_L/μ_R on the order of $\pm 5\,\mu$eV. The plunger gate voltages are set with a resolution of $60\,\mu$V, which combined with a QD leverarm of ≈ 0.05 would translate to potential offsets on the order of $3\,\mu$eV in μ_L and μ_R. **e**-**h**. shows a repetition of the outlined procedure, for measurements using the charge configuration shown in Extended Data Fig. 11. A similar behaviour is observed.

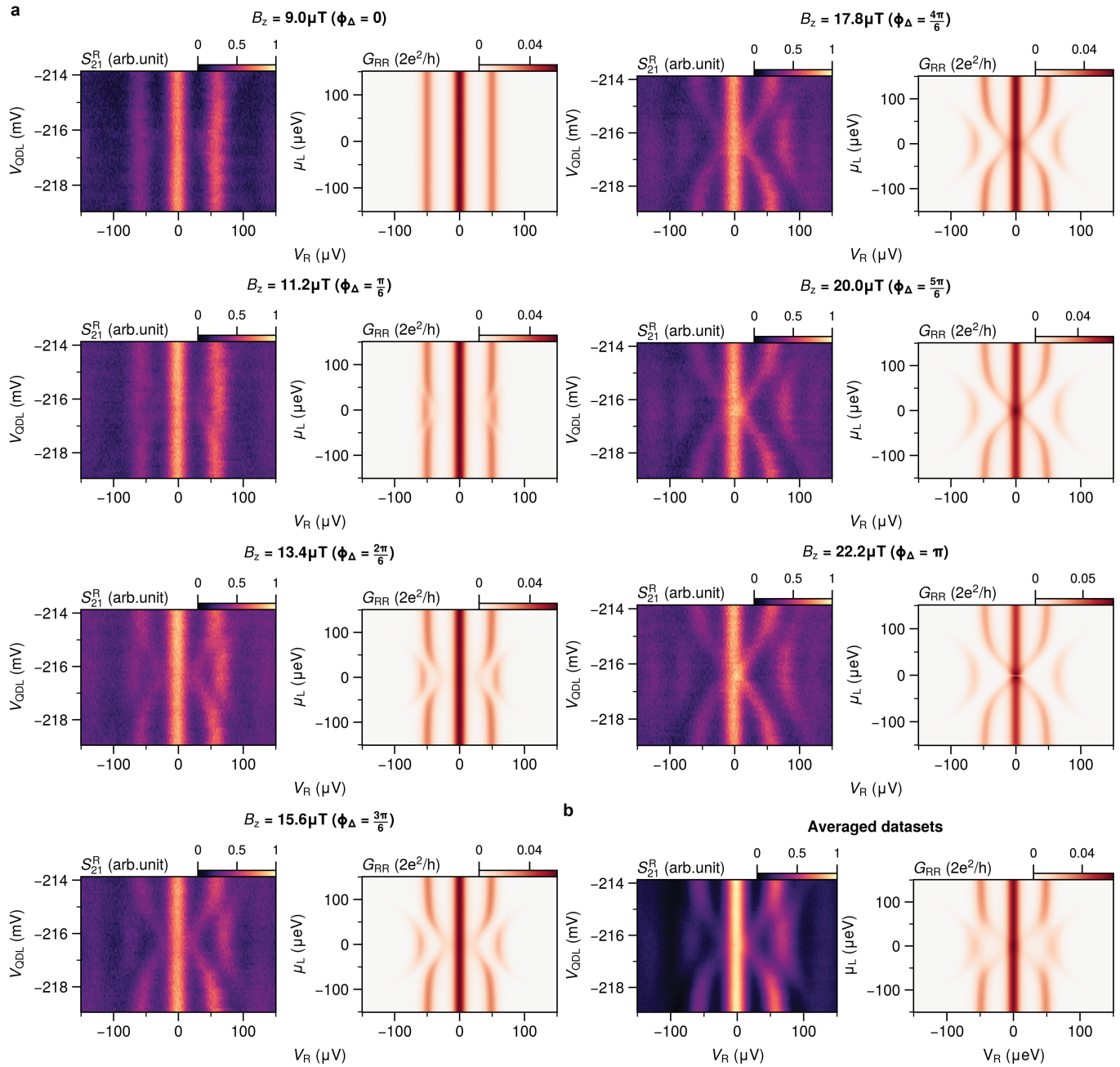

Extended Data Fig. 6 | Conductance spectra for ϕ_Δ between 0 and π. In the main text, Fig. 3 shows measurements of conductance spectra at a three-site sweet spot, obtained at two B_z values corresponding to $\phi_\Delta = 0$ and $\phi_\Delta = \pi$. The ability to control the flux allows us to perform such measurements at any intermediate value of ϕ_Δ. **a**. RF-spectroscopy measurements of S_{21}^R and corresponding numerical simulations, upon detuning V_{QDL}, for seven values of B_z corresponding to $\phi_\Delta = 0$ and $\phi_\Delta = \pi$. The experimental evolution corresponds well to the numerical simulation at each stage. Recent work on a three-site Kitaev chain with two separately grounded SCs[24] concludes that a small voltage difference between the SCs (on the order of μV) may give rise to rapid phase oscillations. Hence, it is assumed their (slow) measurements reflect an average over many periods of ϕ_Δ. **b**. Shows averaged RF-spectroscopy for 25 measurements in the same range as (a), and the corresponding numerically averaged simulation, finding good agreement with the reported behaviour in[24].

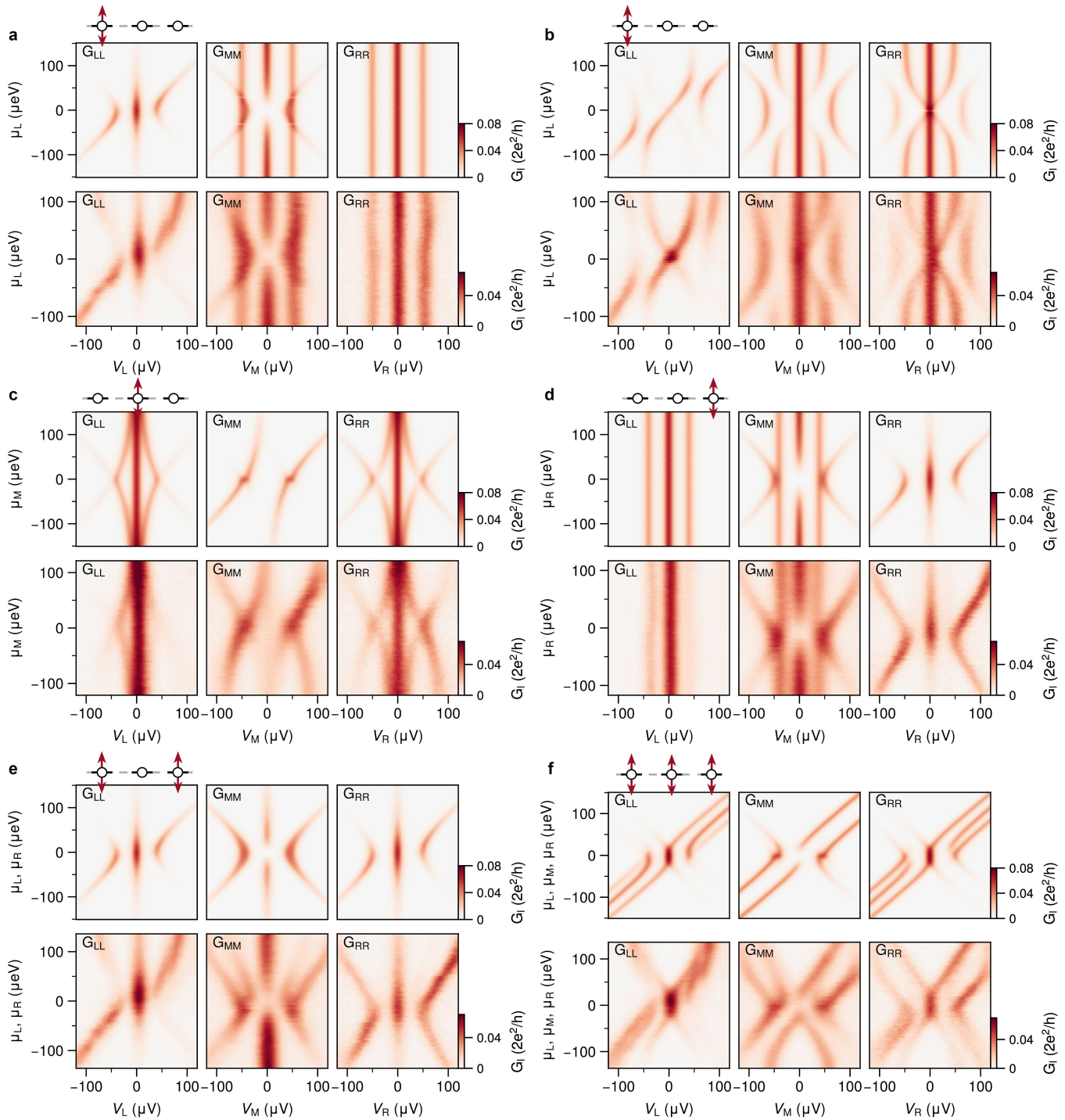

Extended Data Fig. 7 | Three-site conductance spectra for different QD detuning combinations. In a three-site Kitaev chain, the ZBPs arising on the outer QDs are expected to persist when detuning either a single QD or pairs of QDs[24]. Figure 3 only demonstrates the response to detuning V_{QDL}. Here, four other possible detuning combinations are highlighted, for the same device configuration. Accompanying numerical simulations use the same set of parameters as shown in the main text. Plunger gate voltages have been converted to chemical potential energies using the QD leverarms. **a**. and **b**. show repetitions of the conductance spectra shown in Fig. 3, where $\phi_\Delta = 0$ and $\phi_\Delta = \pi$ respectively, including a comparison to the numerical simulation. Furthermore, we show the response at $\phi_\Delta = 0$ to **c**. Detuning V_{QDM} (μ_M), **d**. detuning V_{QDR} (μ_R), **e**. detuning both V_{QDL} and V_{QDR} and **f**. detuning all three QDs simultaneously. When $\phi_\Delta = 0$, the ZBP measured in G_{LL} and G_{RR} only splits from zero-energy when all three QDs are detuned.

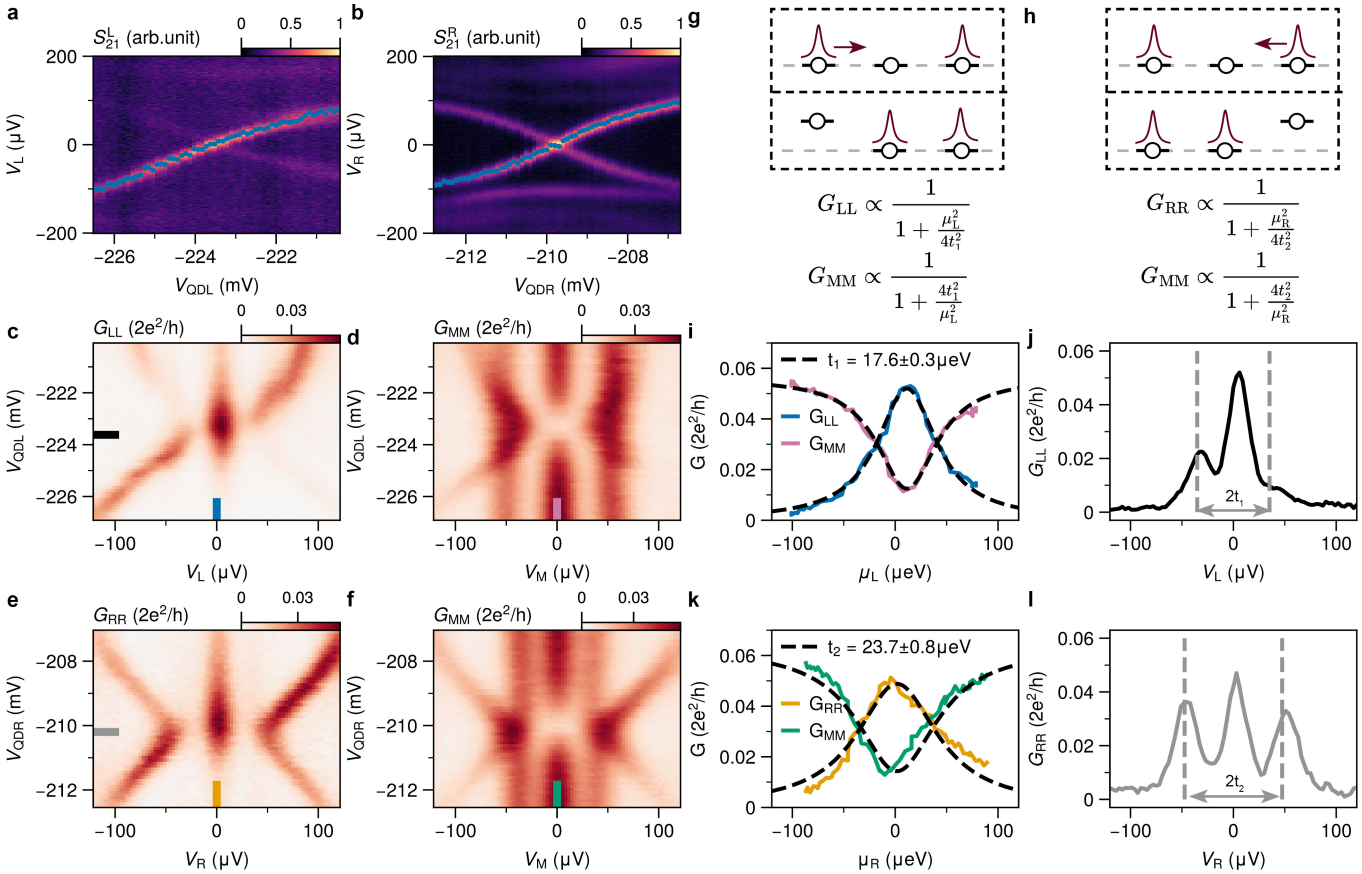

Extended Data Fig. 8 | Shifting the MBS wavefunction - comparison to analytical result. At a three-site Kitaev chain sweet spot, with $\phi_4 = 0$, detuning either of the outer QDs shifts the MBS wave-function to the middle QD. In Methods, we derive that this reflects in the zero-bias conductance of each site and depends only on the coupling parameters t_1/t_2 (= Δ_1/Δ_2) (see Eqs. (16)). To do this analysis experimentally, first the chemical-potential energies μ_L, μ_R of QDL and QDR are measured as a function of **a**. V_{QDL} and **b**. V_{QDR}, by measuring each QD spectrum with the unused QDs in Coulomb blockade. With all parameters tuned to the sweet spot values, we detune V_{QDL} around charge degeneracy and measure **c**. G_{LL} and **d**. G_{MM}, as shown in Fig. 3a. Additionally, we detune V_{QDR} and measure **e**. G_{RR} and **f**. G_{MM}. As visualised in **g**. and **h**., these experiments result in the shifting of the MBS wave-function from the outer QD to the inner QD. In (c,d), the conductances measured at $V_L, V_M = 0$ depend only on μ_L and t_1. Similarly for (e,f) they scale according to μ_R and t_2. **i**. We extract G_{LL} and G_{MM} along $V_L, V_M = 0$ from (c) and (d) and convert V_{QDL} to μ_L using (a). Fitting the analytical formulas shown in (g), with an additional scaling factor, an estimate for t_1 of 17.6 μeV is obtained. This can be compared to the width of the excitation gap at $\mu_L = 0$, which theory predicts to be $2t_1$. **j**. shows the line-trace, with the dashed lines indicating the expected location of the excited states based on the extraction in (i). **k**. We repeat this procedure for G_{RR} and G_{MM} along $V_R, V_M = 0$ from (e) and (f), converting V_{QDL} to μ_R using (b). Now fitting the formulates shown in (h), we can estimate t_2 of 23.7 μeV. **l**. This again agrees with the excitation gap at $\mu_R = 0$.

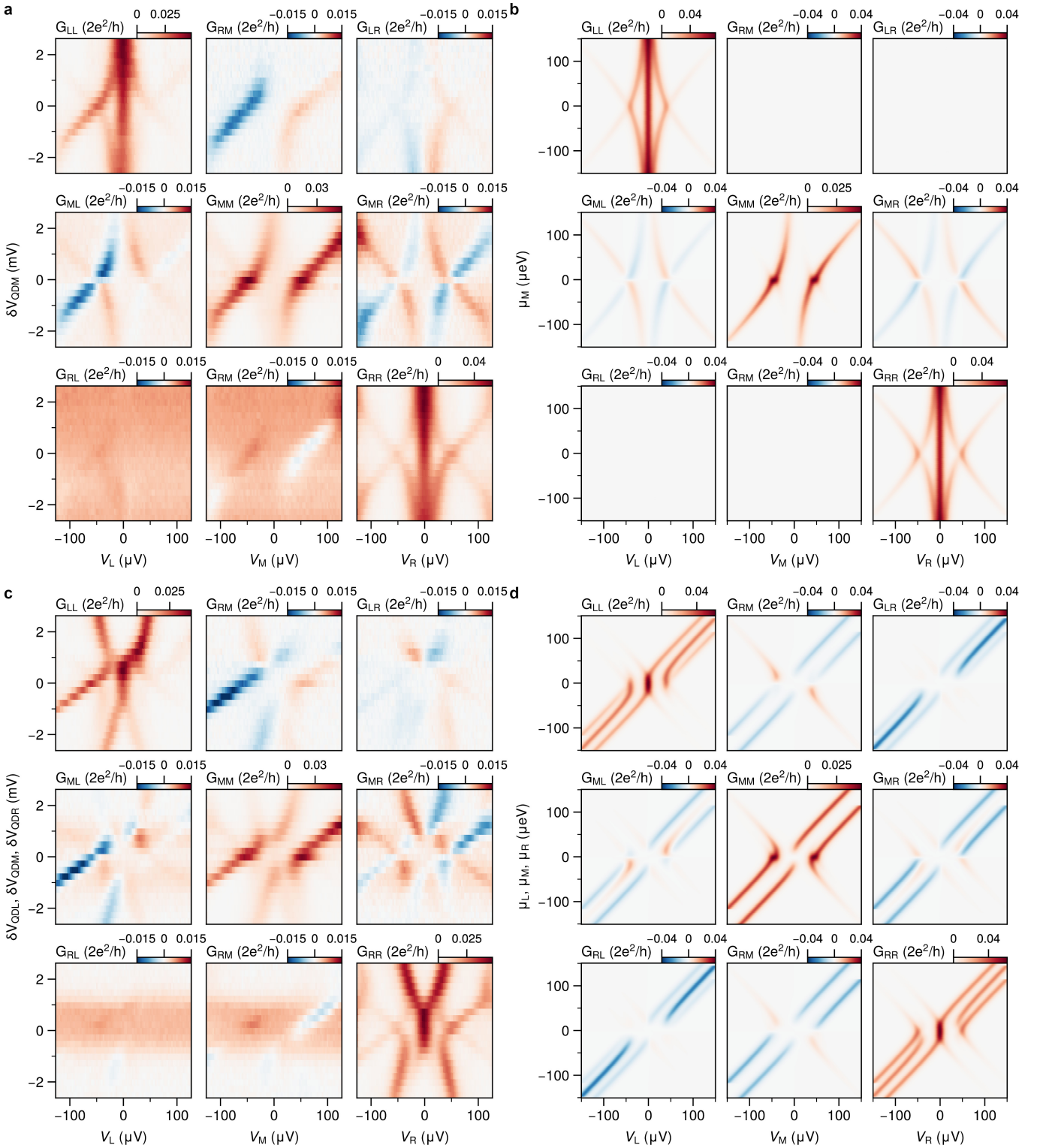

Extended Data Fig. 9 | Full local and non-local conductance matrix measurements. The main text focuses on measurements of local conductances probed through each of the three normal contacts. For such measurements, the non-local responses are recorded in addition, not shown due to size constraints. Here two measurements are highlighted, for the charge configuration shown in Extended Data Fig. 4g. **a**. Local and non-local conductances when detuning V_{QDM}, compared to **b**. numerical simulations of detuning μ_M. Strikingly, the ZBPs do not appear in the non-local measurements, as expected due to arising from MBSs localised on the outer QDs. Additionally, the same patterns of positive and negative non-local conductance in G_{ML} and G_{LM} are observed, with the sign inverting at $\mu = 0$. Unlike the simulations, signals appear in G_{RM}, G_{LR}, G_{RL} and G_{RM} that are not captured by the effective model. We note that a more complete model incorporating explicitly the hybrid regions such as in[30] may be needed to fully describe all non-local effects. **c**. Local and non-local conductances when simultaneously detuning V_{QDL}, V_{QDM} and V_{QDR}, compared to **d**. numerical simulations of detuning all μ_i.

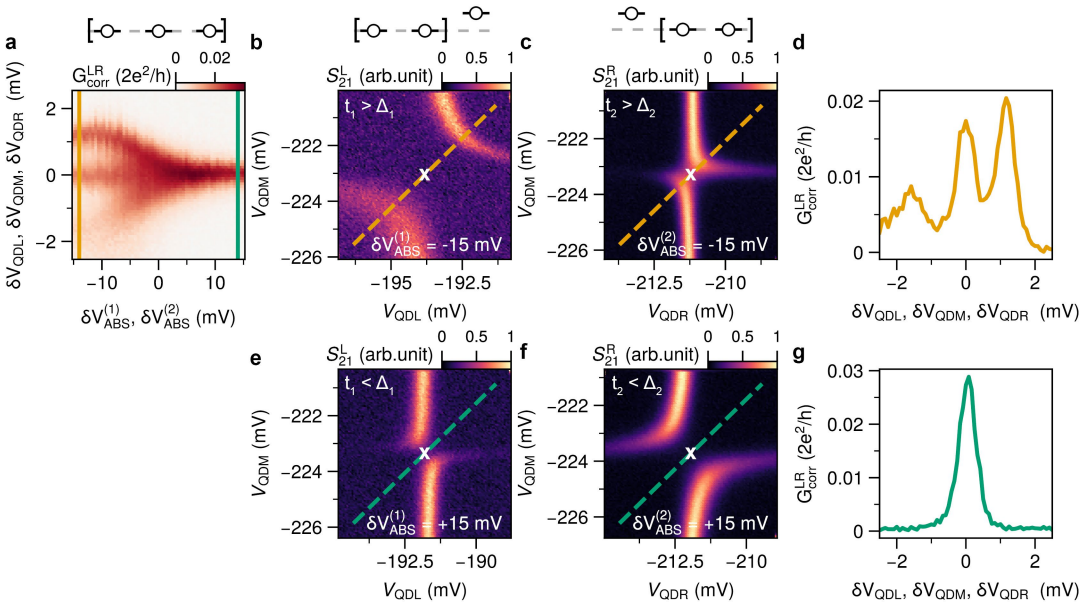

Extended Data Fig. 10 | Details of measurement procedure for Fig. 4. In the main text, Fig. 4 highlights zero-bias conductance measurements at a three-site sweet spot, when simultaneously varying V_{QDL}, V_{QDM} and V_{QDR} against simultaneously sweeping $V^{(1)}_{ABS}$ and $V^{(2)}_{ABS}$. Here, we detail how these measurements are performed. **a**. shows a repetition of the data as shown in Fig. 4e. First, the sweet spot values for $V^{(1)}_{ABS}$ and $V^{(2)}_{ABS}$ were determined from measuring CSDs, through the process shown in Fig. 1. We denote these values $\delta V^{(1)}_{ABS} = 0$ and $\delta V^{(2)}_{ABS} = 0$ respectively. Next, we apply 15 mV to each, with respect to these sweep spot voltages, in the direction that results in an avoided crossing signifying $t > \Delta$. Due to cross-coupling, the resonance value for each QD needs to be re-determined. This is done by measuring the zero-bias Coulomb resonance for each QD, with the two other QDs set off resonance, and fitting a Lorentzian line-shape to determine the centre. **b**. and **c**. show CSDs measured at these V_{ABS} values for the left-middle and middle-right pairs respectively, taken for verification of the interdot coupling. Both sides show an antidiagonal avoided crossing signifying $t_i > \Delta_i$. The centers as obtained by the centering procedure are marked by the crosses. After centering, all three QDs are brought on resonance and swept simultaneously, accounting for differences in leverarms (see Extended Data Fig. 8). Here the orange line-trace in (a) is obtained, shown in **d**. The same procedure is repeated for every set-point, until reaching $V^{(1)}_{ABS}, V^{(2)}_{ABS} = +15$ mV. Now both CSDs show a clear diagonal avoided crossing, shown in **e**. and **f**. The new centers are marked, differing within a few mV from those in (b)/(c). The green dashed lines mark the paths taken by the simultaneous sweep for the green line in (a), plotted in **g**.

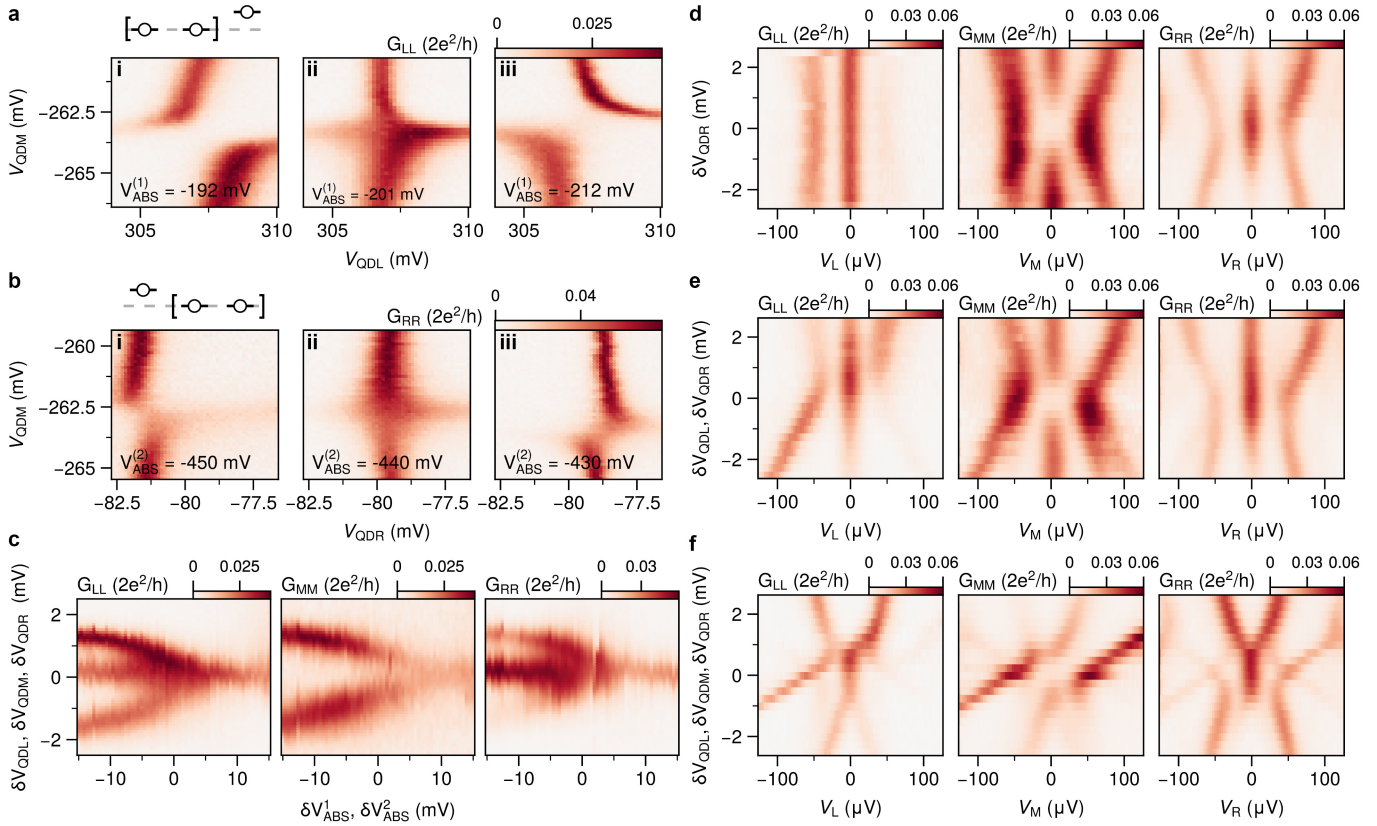

Extended Data Fig. 11 | Reproduction of main results in a separate cooldown. The measurements in Fig. 4 were repeated for validation during a separate cooldown of the same device. First, two-site sweet spots were obtained for both two-site pairs, as in Fig. 1. **a**. CSDs for resonances in the left and middle QD, varying V^1_{ABS} in a range where the avoided crossing changes direction to determine the sweet spot (panel ii). Similarly, a sweet spot was obtained for the middle and right QD, upon varying V^2_{ABS}, shown in **b**. The magnetic field B_z corresponding to $\phi_\Delta = 0$ was determined from the spectroscopy measurements shown in Extended Data Fig. 5g. **c**. In this configuration, the measurement shown in Fig. 4 was repeated, using the same procedure as detailed in Extended Data Fig. 10. Additionally, we reproduce here the conductance spectra at the sweet spot as a function of **d**. detuning V_{QDR}, **e**. detuning both V_{QDL} and V_{QDR} and **f**. detuning simultaneously all 3 QDs.